



WiFi-CSI Difference Paradigm: Achieving Efficient Doppler Speed Estimation for Passive Tracking

WENWEI LI, Peking University, China

RUIYANG GAO, Peking University, China

JIE XIONG, Microsoft Research Asia, China and University of Massachusetts Amherst, USA

JIARUN ZHOU, Peking University, China

LEYE WANG, XINGJIAN MAO, and ENZE YI, Peking University, China

DAQING ZHANG*, Peking University, China and Institut Polytechnique de Paris, France

Passive tracking plays a fundamental role in numerous applications such as elderly care, security surveillance, and smart home. To utilize ubiquitous WiFi signals for passive tracking, the Doppler speed extracted from WiFi CSI (Channel State Information) is the key information. Despite the progress made, existing approaches still require a large number of samples to achieve accurate Doppler speed estimation. To enable WiFi sensing with minimum amount of interference on WiFi communication, accurate Doppler speed estimation with fewer CSI samples is crucial. To achieve this, we build a passive WiFi tracking system which employs a novel CSI difference paradigm instead of CSI for Doppler speed estimation. In this paper, we provide the first deep dive into the potential of CSI difference for fine-grained Doppler speed estimation. Theoretically, our new design allows us to estimate Doppler speed with just three samples. While conventional methods only adopt phase information for Doppler estimation, we creatively fuse both phase and amplitude information to improve Doppler estimation accuracy. Extensive experiments show that our solution outperforms the state-of-the-art approaches, achieving higher accuracy with fewer CSI samples. Based on this proposed WiFi-CSI difference paradigm, we build a prototype passive tracking system which can accurately track a person with a median error lower than 34 cm, achieving similar accuracy compared to the state-of-the-art systems, while significantly reducing the required number of samples to only 5%.

CCS Concepts: • Human-centered computing → Ubiquitous and mobile computing systems and tools.

Additional Key Words and Phrases: Passive Tracking, Doppler Speed Estimation, WiFi Sensing

ACM Reference Format:

Wenwei Li, Ruiyang Gao, Jie Xiong, Jiarun Zhou, Leye Wang, Xingjian Mao, Enze Yi, and Daqing Zhang. 2024. WiFi-CSI Difference Paradigm: Achieving Efficient Doppler Speed Estimation for Passive Tracking. *Proc. ACM Interact. Mob. Wearable Ubiquitous Technol.* 8, 2, Article 63 (June 2024), 29 pages. <https://doi.org/10.1145/3659608>

*Corresponding author.

Authors' Contact Information: Wenwei Li, Key Laboratory of High Confidence Software Technologies (Ministry of Education), School of Computer Science, Peking University, Beijing, China, lwenwei@pku.edu.cn; Ruiyang Gao, Peking University, Beijing, China, gry@pku.edu.cn; Jie Xiong, Microsoft Research Asia, Shanghai, China and University of Massachusetts Amherst, Amherst, USA, jxiong@cs.umass.edu; Jiarun Zhou, Peking University, Beijing, China, jiarun.zhou.01@gmail.com; Leye Wang, Xingjian Mao; Enze Yi, Peking University, Beijing, China, leyewang@pku.edu.cn, 2100012757@stu.pku.edu.cn, yienze_cs@pku.edu.cn; Daqing Zhang, Key Laboratory of High Confidence Software Technologies (Ministry of Education), School of Computer Science, Peking University, Beijing, China, SAMOVAR Lab, Telecom SudParis and Institut Polytechnique de Paris, Paris, France, dqzhang@sei.pku.edu.cn.

Permission to make digital or hard copies of all or part of this work for personal or classroom use is granted without fee provided that copies are not made or distributed for profit or commercial advantage and that copies bear this notice and the full citation on the first page. Copyrights for components of this work owned by others than the author(s) must be honored. Abstracting with credit is permitted. To copy otherwise, or republish, to post on servers or to redistribute to lists, requires prior specific permission and/or a fee. Request permissions from permissions@acm.org.

© 2024 Copyright held by the owner/author(s). Publication rights licensed to ACM.

ACM 2474-9567/2024/6-ART63

<https://doi.org/10.1145/3659608>

1 INTRODUCTION

Alongside the great success of WiFi communication, WiFi-based tracking and sensing have attracted a tremendous amount of attention in the past decade. By utilizing WiFi infrastructure that has already been widely deployed, both active and passive human tracking have been achieved [10, 13, 16, 38, 39, 41, 48]. Compared to active tracking, passive tracking does not require the target to carry any devices.

The basic principle of passive tracking is to extract one or more pieces of information, including distance, angle, and Doppler speed, from signals reflected from the target. While distance and angle information provide important spatial contexts of the target, Doppler speed presents us the target's motion information. However, constrained by the relatively small channel bandwidth, the distance information obtained using WiFi signals is coarse [13, 16]. Limited by the small number of antennas (e.g., 2–4) at commodity WiFi access points, the precision of the angle information is also insufficient for fine-grained tracking [16, 29]. In contrast, the precision of Doppler speed estimates is not constrained by protocol-specified bandwidth or hardware. As long as we have a sufficient number of signal samples from a large-enough time window, theoretically we can obtain accurate Doppler speed information. Therefore, Doppler speed plays an important role in most passive tracking systems [16, 19, 22, 23, 34, 38] based on commodity WiFi devices.

Two methods [31, 42] are widely adopted to obtain signal's Doppler speed information. The first one is converting raw signal samples from time domain to frequency domain through the Fast Fourier Transform (FFT) operation [3, 31, 36]. However, to obtain an accurate estimate, FFT operation requires signal samples from a large time window (e.g., several seconds). In real-world applications, the target speed changes over time and we can not assume a constant target speed within such a long period of time. The second method is to directly calculate the signal phase change rate to obtain the Doppler speed and this method does not require a large time window.

Owing to a higher accuracy, the second method is more widely used for Doppler speed estimation of daily objects. However, the second method still faces one critical challenge, i.e., static signal components (e.g., signals reflected from walls) affect the accuracy of Doppler estimation and they need to be removed. Existing works estimate the static signal components by assuming the dynamic signal components can be averaged out [16, 23, 38, 42]. However, there are two issues associated with existing solutions.

- First, the dynamic signal components can be averaged out only if movement-induced signal phase variation rotates at least a full cycle of 360 degrees. This assumption is not valid in a lot of real-world applications.
- A large number of samples need to be collected to accurately estimate the static signal components. These large number of transmitted samples dedicated for sensing unavoidably affect the communication of WiFi which is a medium-share protocol.

Existing methods [19, 23] typically estimate Doppler speeds with a sampling rate of 1000 Hz. Based on our experiment result shown in Figure 1, transmitting 1000 packets per second for tracking can decrease the data throughput of WiFi communication by more than 90%. This rapid drop in data throughput arises from the Carrier Sense Multiple Access with Collision Avoidance (CSMA/CA) mechanism [5] inherently adopted by IEEE 802.11 WiFi standard. Before a WiFi device transmits a packet, it needs to check if any other WiFi device is transmitting. If so, the channel is considered “busy” and it needs to postpone its transmission to avoid collision. The duration of this postponement grows exponentially with the number of times “busy” channel is detected [1]. As a result, when a large number of WiFi packets (e.g., 200 packets per second) are transmitted for sensing, WiFi devices intended for data transmission would frequently detect a “busy” channel and need to postpone the transmission, leading to a significant drop of data throughput as shown in Figure 1.

To address these issues, in this paper, we propose to use CSI difference rather than CSI for Doppler speed estimation. This new design removes the requirement of 360-degree phase rotation for static component estimation. The CSI differencing operation effectively eliminates the static components of CSI leveraging the fact that static signal components changes slowly and we can safely assume the static components are the same for two CSI

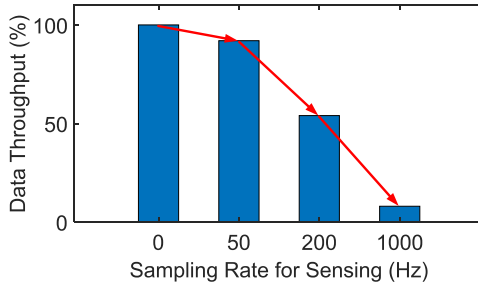


Fig. 1. Impact of number of samples per second on WiFi communication.

samples within a short time interval. Although the differencing operation is straightforward and widely applied, *we are the first to conduct an in-depth investigation into the relationship between CSI difference and Doppler speed*. Our solution presents a new angle to accurately estimate Doppler information using fewer samples.

We propose a TD-CSI (Time-domain Difference of CSI) model to derive the mathematical expression to estimate the Doppler speed using CSI difference instead of CSI. Through a novel double-difference operation, we show that theoretically, one Doppler speed estimate requires a minimum number of three (lower bound) CSI samples. Compared to traditional methods only utilizing signal phase for fine-grained Doppler speed estimation [7, 33, 42], we creatively utilize both amplitude and phase information of CSI difference to increase the estimate accuracy. Specifically, we show that not just signal¹ phase, but signal amplitude also contains Doppler information. What is more exciting is that we religiously prove under the same noise level, the Doppler information contained in signal amplitude is more accurate than that contained in signal phase. However, obtaining Doppler information from signal amplitude is not trivial. We show that while we can obtain the relative Doppler variation pattern from signal amplitude, the absolute Doppler value can not be estimated. The key observation enabling us to address this issue is that although the Doppler information obtained from signal phase is coarse, we can leverage the signal phase to accurately scale the relative Doppler value obtained from signal amplitude to the true absolute Doppler value. This novel design helps us achieve accurate Doppler speed estimation with fewer number of samples (i.e., approaching the theoretical lower bound).

Based on the proposed TD-CSI model, a sensing framework named FewSense is proposed to extract high-precision Doppler speed estimates. Our framework constructs the TD-CSI signal by taking the difference between two CSI samples with a carefully-selected time interval in between. The carefully selected time interval further enhances the robustness of the Doppler speed estimation, ensuring it adapts to velocity changes. To demonstrate the superiority of the proposed framework, we conduct comprehensive experiments in various scenarios. The experiment results show that our method can achieve accurate Doppler speed estimation using only 5% of the samples required by the state-of-the-art methods. We further build a prototype passive tracking system based on our framework. Our system enables accurate human tracking with a sampling rate of only 50 Hz, compared with a sampling rate of 1000 Hz in the state-of-the-art systems [19, 23], significantly mitigating the interference induced by sensing on communication.

To summarize, we made the following contributions.

- We propose to use CSI difference instead of CSI for Doppler speed estimation. We establish the rigorous mathematical relationship between CSI difference and Doppler speed for the first time.
- Based on the model proposed, we derive the theoretical lower bound of the number of samples required for Doppler speed estimation.

¹Note that here signal is referring to CSI difference rather than CSI.

- We propose a novel scheme to combine both signal phase and amplitude to improve the estimation accuracy, lowering the number of samples required for Doppler estimation in practice. Our design can greatly reduce the interference of WiFi sensing on communication, moving one step towards real-life adoption of Doppler speed for tracking.
- We conduct extensive experiments to demonstrate the effectiveness of the proposed system. The result shows that our method outperforms the state-of-the-art approaches, and our prototype system achieves similar tracking accuracy compared to the state-of-the-art systems, while significantly reducing the required number of samples to only 5%. The demo video can be found at: <https://youtu.be/5fQi2mSYbwA>.

The rest of this paper is organized as follows. We present the research background in Section 2 and explain why prior works fail to obtain accurate Doppler speed estimates in real-world settings. Then, we establish TD-CSI model in Section 3 and explore its properties for Doppler speed estimation. In Section 4 we design the Doppler speed estimation framework based on the proposed TD-CSI model. We conduct comprehensive experiments to evaluate the performance of our proposed method in Section 5. In Section 6 we discuss the limitations and potential of our work. We survey the related work in Section 7 and conclude our work in Section 8.

2 BACKGROUND

In this section, we first introduce the basics of Doppler speed estimation using WiFi CSI. Then, we analyze the challenges associated with accurately estimating Doppler speed with few CSI samples.

2.1 Estimating Doppler speed with CSI

WiFi signals propagate through multiple paths from the transmitter to the receiver in the environment. The WiFi CSI characterizes the propagation channel and is the superposition of the components from all paths. CSI can be divided into static, dynamic, and noise components. The static component contains Line-of-Sight (LoS) path and environmental reflections, which are not related to the moving target. The dynamic component represents the paths reflected from the moving target, and is simplified into one equivalent path when there is a single target. Note that for the dynamic component of CSI, usually only the one-bounce signal reflected from the target is considered because the multi-bounce reflections are too weak to be used for sensing and are usually considered as noise [7, 15]. The noise component is composed of thermal noise and background interference. Therefore, CSI can be represented as [7, 32, 43, 45]

$$H(t) = H_s + Ae^{-j2\pi \frac{d(t)}{\lambda}} + \epsilon(t), \quad (1)$$

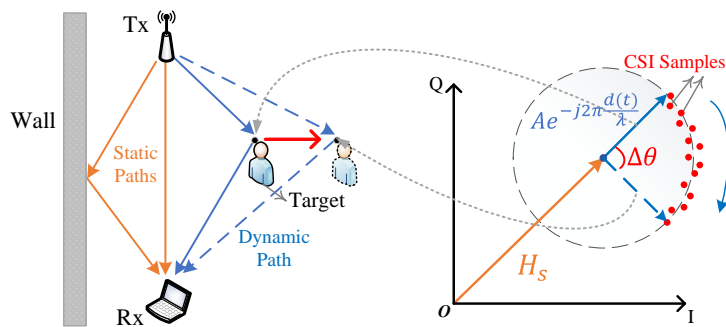


Fig. 2. Illustration of the relationship between CSI and target motion.

where H_s denotes the static CSI component, A and $-2\pi \frac{d(t)}{\lambda}$ denote the amplitude² and phase of the dynamic CSI component, respectively. $d(t)$ denotes the length of the path reflected by the target and λ is the wavelength of the transmitted signal. $\epsilon(t)$ denotes the noise component, which is modeled as a random variable following a zero-mean distribution [7, 17, 47].

As shown in Figure 2, when the target moves, the path length $d(t)$ changes, causing the dynamic CSI component to continuously change and form a circular arc on the complex I-Q plane. Due to random noise, the CSI samples are distributed around this circular arc.

The Doppler speed of the target is the change rate of the signal path length $d(t)$. Based on Equation 1, the Doppler speed (denoted as $v_d(t)$) can be calculated as

$$v_d(t) = \frac{\Delta d(t)}{\Delta t} = -\frac{\lambda \cdot \Delta\theta(t)}{2\pi\Delta t}, \quad (2)$$

where $\Delta\theta(t) = -2\pi \frac{\Delta d(t)}{\lambda}$ is the phase variation of the dynamic CSI component during an interval of Δt , corresponding to the rotation angle of the circular arc shown in Figure 2. By extracting the phase variation of the dynamic CSI component, we can obtain Doppler speed estimates of the target.

2.2 Challenges of Accurate Doppler Speed Estimation using Few CSI Samples

As presented in Equation 2, to obtain Doppler speed estimates from CSI, we need to extract the phase variations of the dynamic CSI component (denoted as $\Delta\theta(t)$). However, the presence of unknown static components in CSI makes the extraction of $\Delta\theta(t)$ not trivial. It is necessary to eliminate the impact of the unknown static components before we can extract $\Delta\theta(t)$. To this end, existing works [16, 23, 38, 42] propose various approaches for static component removal. For these approaches, quite a few CSI samples are required to ensure the accuracy of the statistical results of the static component estimation. More importantly, some assumptions need to be met for these approaches to work. In the following, we use examples to illustrate the limitations of these approaches.

IndoTrack [16] estimates Doppler speed with the conjugate product of the CSI sampled from two antennas. By adjusting the power of each antenna [16], the conjugate product can be expressed in the same form as CSI in Equation 1. Since the conjugate product also rotates along a circle on the complex plane, IndoTrack estimates the static component as the mean value of the conjugate products within a period of time, assuming that the conjugate product rotates at least one full cycle of 360 degrees during this period and the dynamic components

²The amplitude A can be considered as a constant within a small time window (e.g., 0.5 second) and the phase variation is more significant.

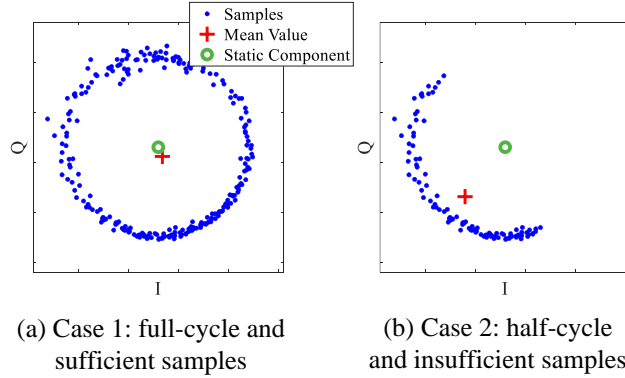


Fig. 3. Illustration of the bias in estimating the static component in two different cases.

can be averaged out. However, since the amount of rotation depends on the target displacement, the conjugate products do not necessarily rotate a full cycle. Also, when the target changes its direction of movement, the rotation direction also changes, further reducing the chance of rotating a full cycle. Moreover, when the target speed is not high, it takes a relatively long time to have a full cycle of phase rotation, causing a large latency in the calculation. Figure 3 shows the mean value and the true static components in two different cases. In Figure 3(a), the conjugate product rotates almost a full cycle and the mean value is close to the true static component in this case. However, as shown in Figure 3(b), the mean value deviates significantly from the true static component when the conjugate product only rotates half cycle. QGesture [42] adopts a similar method to estimate the static component. QGesture estimates the static component of CSI as the mean of the last pair of local maximum and minimum values. However, unexpected local maximum (or minimum) values can severely degrade the estimation accuracy.

To conclude, existing works require a large number of CSI samples to remove the static component. In our work, we eliminate the static component solely based on its inherent property without a need of this requirement. Our approach constructs a new base signal (TD-CSI) and establishes its relationship with Doppler speed, laying the theoretical foundation for future research.

3 UNDERSTANDING TD-CSI MODEL FOR DOPPLER SPEED ESTIMATION

In this section, we first introduce TD-CSI as a base signal. Then, we model TD-CSI and establish its relationship with Doppler speed. We further derive Doppler speed estimates from both the amplitude and phase of TD-CSI and analyze the estimation errors. Subsequently, we determine the theoretical minimum number of samples required for Doppler speed estimation using TD-CSI. Finally, we verify the proposed TD-CSI model through benchmark experiments.

3.1 TD-CSI: A Base Signal Independent of the Static CSI Component

As indicated by Equation 1 and Equation 2, eliminating the static component in CSI is an essential step for Doppler speed estimation. To achieve this, we exploit the inherent property of the static component to eliminate it.

The static component of CSI changes slowly [34, 42]. This means that two CSI samples taken within a short period of time have identical static components. By taking the difference between these two samples, we can effectively eliminate the static component. With Equation 1, the difference between the two CSI samples, i.e., TD-CSI (denoted as $D(t)$), can be expressed as

$$\begin{aligned} D(t) &= H(t + \Delta t) - H(t) = \Delta H_s + \Delta(Ae^{-j2\pi\frac{d(t)}{\lambda}}) + \Delta\epsilon(t) \\ &= \Delta(Ae^{-j2\pi\frac{d(t)}{\lambda}}) + \Delta\epsilon(t), \end{aligned} \quad (3)$$

where Δt is the time interval between two selected CSI samples. As expressed in Equation 3, TD-CSI consists of the differences of the static component, dynamic component, and noise component. Since the difference of the static component is close to 0, TD-CSI is independent of the static CSI component. What remains in TD-CSI are the differences of the dynamic component and the noise component. Thus, TD-CSI inherently eliminates the static CSI component, while preserving the Doppler speed information in the dynamic CSI component, albeit in a different form. Aiming to accurately estimate Doppler speed, we proceed to establish the mathematical relationship between TD-CSI and the Doppler speed.

3.2 Relationship Between TD-CSI and the Doppler Speed

We further derive the relationship between TD-CSI and Doppler speed based on Equation 3. TD-CSI consists of the target component and the noise component. While the noise component is independent of the Doppler speed, we focus on the target component.

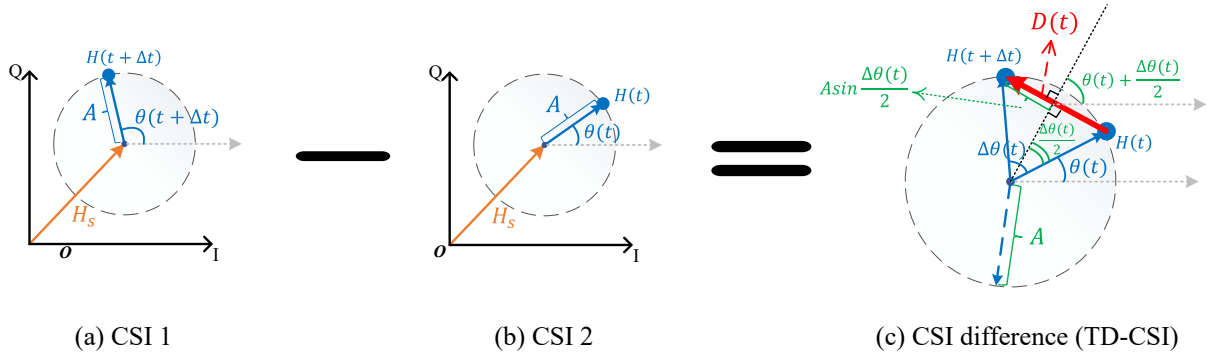


Fig. 4. Illustration of the TD-CSI model. (a) CSI sampled at $t + \Delta t$; (b) CSI sampled at t ; (c) TD-CSI (represented by the red vector), i.e., the difference between the two CSI vector samples. Note that we omit the noise components of CSI and TD-CSI for simplicity.

The target component of TD-CSI is the difference of the dynamic CSI component. To simplify our analysis, we denote the phase of the dynamic CSI component (i.e., $-2\pi \frac{d(t)}{\lambda}$) as $\theta(t)$ in the following and the dynamic component of CSI is thus denoted as $Ae^{j\theta(t)}$. On the complex plane, $Ae^{j\theta(t)}$ moves on a circle of radius A as the target moves. Therefore, the target component of TD-CSI, i.e., $\Delta(Ae^{j\theta(t)})$, is the difference between two complex values on the circle. As illustrated in Figure 4, the target component of TD-CSI can be represented as a directed chord on the circle. Based on the rigorous geometric derivation shown in Figure 4, TD-CSI ($D(t)$) can be represented as

$$D(t) = 2A \sin \frac{\Delta\theta(t)}{2} e^{j(\theta(t) + \frac{\Delta\theta(t)}{2} + \frac{\pi}{2})} + \Delta\epsilon(t), \quad (4)$$

where $\Delta\theta(t) = \theta(t + \Delta t) - \theta(t)$ represents the phase variation of the dynamic CSI component during the time interval of Δt . To further establish the relationship between TD-CSI and Doppler speed, we derive the expressions for both the amplitude and phase of TD-CSI as

$$|D(t)| = 2A |\sin \frac{\Delta\theta(t)}{2}| + \epsilon_a(t), \quad (5)$$

$$\angle D(t) = \theta(t) + \frac{\Delta\theta(t)}{2} + \frac{\pi}{2} + \pi \cdot [\Delta\theta(t) < 0] + \epsilon_p(t), \quad (6)$$

where $\epsilon_a(t)$ and $\epsilon_p(t)$ represent the projections of the noise component onto the amplitude and phase of TD-CSI, respectively. $\epsilon_p(t)$ follows a zero-mean distribution.

Note that the Doppler speed can be readily determined with $\Delta\theta(t)$ as expressed in Equation 2. Therefore, the relationship between TD-CSI and $\Delta\theta(t)$ is essential for Doppler speed estimation. Equation 5 and Equation 6 indicate that both the amplitude and phase of TD-CSI are related to $\Delta\theta(t)$, hence we can obtain the first property of TD-CSI as follows:

- **P1:** The amplitude and phase of TD-CSI reflect the Doppler speed of the target from different perspectives.

Therefore, we can derive expressions for the estimates of $\Delta\theta(t)$ from the amplitude and phase of TD-CSI, respectively. Moreover, we further analyze the impact of noise on each of the two estimates.

3.3 Principles of Doppler Speed Estimation using TD-CSI

3.3.1 Expressions of Doppler Speed Estimates. We now derive estimates of $\Delta\theta(t)$ from the amplitude and phase of TD-CSI, respectively. With estimates of $\Delta\theta(t)$, the Doppler speed estimates can be readily determined with Equation 2.

First, based on Equation 5, we can use the amplitude of TD-CSI to estimate the absolute value of $\Delta\theta(t)$ as

$$\widehat{|\Delta\theta(t)|}_a = 2 \arcsin \frac{|D(t)|}{2A}, \quad (7)$$

where $\widehat{|\Delta\theta(t)|}_a$ represents the absolute value of $\Delta\theta(t)$ estimated with the amplitude of TD-CSI. To calculate $\widehat{|\Delta\theta(t)|}_a$ using Equation 7, we require the amplitude of TD-CSI and the additional parameter A , which is the amplitude of the dynamic CSI component. Moreover, we also need to determine the sign of $\Delta\theta(t)$. Later we will analyze the impact of noise on $\widehat{|\Delta\theta(t)|}_a$ and this analysis serves as the motivation of our novel method proposed in Section 4.2.

Now, we move on to use the phase of TD-CSI to estimate $\Delta\theta(t)$. According to Equation 6, the phase of TD-CSI contains both the desired $\Delta\theta(t)$ and the time-varying $\theta(t)$, hindering the estimation of $\Delta\theta(t)$. To tackle this issue, we adopt a double-difference operation to utilize the phase difference of TD-CSI for processing. $\Delta\theta(t)$ remains unchanged for a short period of time, i.e., $\Delta(\Delta\theta(t)) \ll \Delta\theta(t)$. Then, the phase difference of TD-CSI can be expressed as $\Delta(\angle D(t)) = \Delta\theta(t) + \frac{\Delta(\Delta\theta(t))}{2} + \Delta\epsilon_p(t) \approx \Delta\theta(t) + \Delta\epsilon_p(t)$, where $\Delta\epsilon_p(t)$ represents the difference of $\epsilon_p(t)$ and it also follows a zero-mean distribution. Note that the time interval between the TD-CSI phases here is still Δt . The sudden change of π induced by the sign alteration of $\Delta\theta(t)$ (as expressed in Equation 6) is ignored for $\Delta(\angle D(t))$ since the sign of $\Delta\theta(t)$ remains unchanged in most cases. With the phase difference of TD-CSI, we can estimate $\Delta\theta(t)$ as

$$\widehat{\Delta\theta(t)}_p = \Delta(\angle D(t)), \quad (8)$$

where $\widehat{\Delta\theta(t)}_p$ represents $\Delta\theta(t)$ estimated with the phase difference of TD-CSI. Equation 8 indicates that we can estimate $\Delta\theta(t)$ using only the phase difference of TD-CSI, without a need of any additional parameters.

To sum up, we can obtain the second property of TD-CSI as follows:

- **P2:** Estimating Doppler speed using the amplitude of TD-CSI requires additional parameters, whereas the phase of TD-CSI allows for direct estimation of Doppler speed.

3.3.2 Impact of Noise on the Doppler Speed Estimates. We now investigate the impact of random noise on the estimates of $\Delta\theta(t)$. Random noise in TD-CSI amplitude and phase cause errors in the estimates of $\Delta\theta(t)$. Both the amplitude and phase noises originate from the noise component of TD-CSI (i.e., $\Delta\epsilon(t)$). To facilitate further analysis, we assume that the distribution of the noise $\Delta\epsilon(t)$ is circularly symmetric. Prior work [7] offers support for this assumption, and we further carry out an empirical study in Appendix A.1 to confirm this assumption about the noise distribution. Without loss of generality, we further fix the amplitude of $\Delta\epsilon(t)$ as σ . Then $\Delta\epsilon(t)$ is distributed on a circle with radius σ on the complex plane. Figure 5(a) illustrates the case where $\Delta\epsilon(t)$ has the maximum impact on the amplitude of TD-CSI. With Equation 7, we can derive the maximum error of $\widehat{|\Delta\theta(t)|}_a$ (denoted as $ME(\widehat{|\Delta\theta(t)|}_a)$) as

$$ME(\widehat{|\Delta\theta(t)|}_a) = 2 \arcsin \frac{2A|\sin \frac{\Delta\theta(t)}{2}| + \sigma}{2A} - |\Delta\theta(t)| \approx \frac{\sigma}{A}, \quad (9)$$

where we take an approximation to help us compare the amplitude error with the phase error later on.

Figure 5(b) illustrates the case where $\Delta\epsilon(t)$ has the maximum impact on the phase of TD-CSI. In this case, the phase shift induced by $\Delta\epsilon(t)$ is $\alpha = \arcsin(\sigma/|2A \sin \frac{\Delta\theta(t)}{2}|)$. Since the phase shifts of two TD-CSI samples are

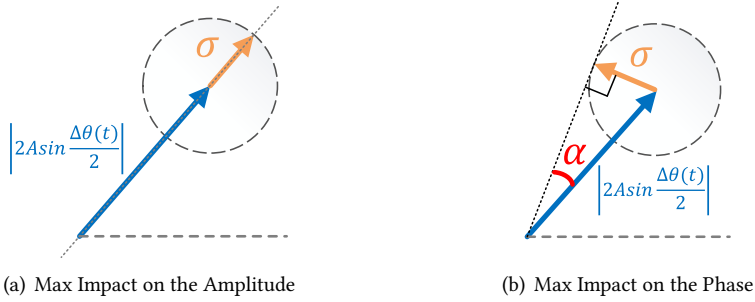


Fig. 5. Illustration of maximum impact of random noise on phase and amplitude.

independent, the maximum shift of the phase difference of TD-CSI is 2α . With Equation 8, we can derive the maximum error of $\widehat{\Delta\theta(t)}_p$ (denoted as $ME(\widehat{\Delta\theta(t)}_p)$) as

$$ME(\widehat{\Delta\theta(t)}_p) = 2 \arcsin \frac{\sigma}{2A|\sin \frac{\Delta\theta(t)}{2}|}. \quad (10)$$

Note that Equation 10 indicates that the magnitude of $\Delta\theta(t)$ affects the accuracy of Doppler speed estimation using the phase of TD-CSI. Specifically, when $\Delta\theta(t) = \pi$, the error of $\widehat{\Delta\theta(t)}_p$ is minimized. As presented in Equation 2, $\Delta\theta(t)$ is related to both the Doppler speed and the time interval Δt used to construct TD-CSI. By selecting the time interval Δt , we can adjust the magnitude of $\Delta\theta(t)$. Thus we can obtain the third property of TD-CSI as follows:

- **P3:** By selecting an appropriate time interval for TD-CSI construction, we can reduce the impact of noise on the phase of TD-CSI.

This property guides us in constructing a TD-CSI signal that less affected by noise, thereby enhancing the accuracy of Doppler speed estimation, as detailed in Section 4.1.

We further compare the impact of noise on $|\widehat{\Delta\theta(t)}|_a$ and $\widehat{\Delta\theta(t)}_p$. Equation 9 and Equation 10 yield inequalities as

$$ME(|\widehat{\Delta\theta(t)}|_a) \approx \frac{\sigma}{A} \leq \frac{\sigma}{A|\sin \frac{\Delta\theta(t)}{2}|} \leq 2 \arcsin \frac{\sigma}{2A|\sin \frac{\Delta\theta(t)}{2}|} = ME(\widehat{\Delta\theta(t)}_p). \quad (11)$$

Equation 11 shows that the maximum error of $|\widehat{\Delta\theta(t)}|_a$ is constantly lower than that of $\widehat{\Delta\theta(t)}_p$. Moreover, when sensing a target with varying position and velocity, there are situations where the Doppler speed of the target approaches zero. This happens, for instance, when the target is stationary or moves parallel to the Fresnel Zone [30, 35]. In such cases, $|\sin \frac{\Delta\theta(t)}{2}| \ll 1$, resulting in $ME(\widehat{\Delta\theta(t)}_p) \gg ME(|\widehat{\Delta\theta(t)}|_a)$, i.e., the maximum impact of random noise on the phase-based Doppler estimate can be significantly greater than its maximum impact on the amplitude-based estimate. Note that, for simplicity in the theoretical derivations, we focus on only the maximum error values in the preceding analysis. Further discussion on the average error values of the amplitude-based versus phase-based estimation is available in Appendix A.2. The takeaway is that the average error of the amplitude-based estimation is also significantly lower than the average error of phase-based estimation. Thus, we can obtain the fourth property of TD-CSI as follows:

- **P4:** The Doppler speed information in the amplitude of TD-CSI is less affected by noise than that in the phase of TD-CSI.

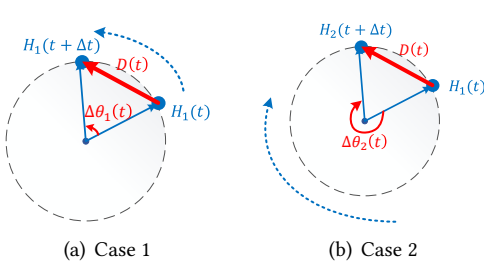


Fig. 6. Illustration of the ambiguity of $\Delta\theta(t)$. Note that we omit the noise components for simplicity.

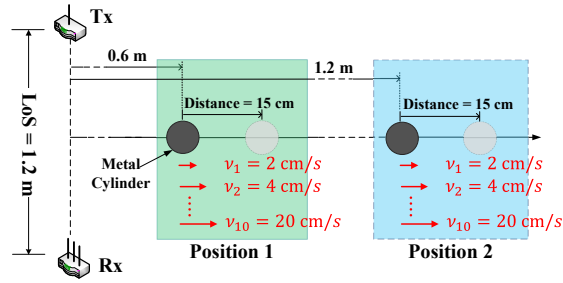


Fig. 7. Settings of the benchmark experiments for verifying the TD-CSl model.

This property motivates us to derive the additional parameters required by the amplitude-based estimation, achieving a more accurate Doppler speed estimation with the TD-CSl amplitude, as detailed in Section 4.2.

3.4 Requirements of Doppler Speed Estimation using TD-CSl

We focus on two sample-related requirements for Doppler speed estimation using TD-CSl.

3.4.1 The Requirement of CSI Sampling Rate. Although Equation 4 holds, ambiguity arises due to phase wrapping of $\Delta\theta(t)$. For example, as shown in Figure 6, $\Delta\theta_1(t) = \Delta\theta_2(t) + 2\pi$, and the target components of TD-CSl are identical in the two cases. To avoid ambiguity, we limit $\Delta\theta(t)$ to $-\pi \leq \Delta\theta(t) < \pi$. To satisfy this, the time interval Δt between the two CSI samples used to construct TD-CSl must follow $|2\pi f_d(t)\Delta t| < \pi$, where $f_d(t) = \frac{\Delta\theta(t)}{2\pi\Delta t} = \frac{v_d(t)}{\lambda}$ denotes the Doppler frequency of the moving target. This condition can be expressed as $\Delta t < \frac{1}{2|f_d(t)|}$. Therefore, to obtain CSI samples that adhere to this time interval constraint, the sampling rate of CSI (f_s) must meet the requirement that $f_s > 2|f_d(t)|$.

3.4.2 The Requirement of Number of CSI Samples. As expressed in Equation 8, we can obtain one Doppler speed estimate with just one phase difference of TD-CSl. To obtain one phase difference value of TD-CSl, two TD-CSl samples are needed. Note that each TD-CSl sample is calculated with two different CSI samples. Therefore, a minimum of three CSI samples are needed to estimate the Doppler speed using TD-CSl.

3.5 Verification of TD-CSl Model

In this subsection, we conduct benchmark experiments to verify our proposed TD-CSl model. The experiments are carried out in an office room with furniture. We use a metal cylinder with a diameter of 20 cm and a height of 20 cm as the moving target. To precisely control the speed of the metal cylinder, we mount the cylinder on a high-precision sliding track, as shown in Figure 13. The transmitter and receiver are placed 1.2 m apart, and we place the sliding track along the perpendicular bisector of the transceiver pair. As illustrated in Figure 7, we uniformly move the cylinder a short distance at various speeds from two different starting positions. We set up the transceiver pair to transmit WiFi packets and collect CSI samples at a frequency of 400 Hz. The central frequency of the WiFi signal is set to 5.50 GHz. We construct TD-CSl using the collected CSI data³ to verify the four properties of TD-CSl derived in the preceding subsections.

3.5.1 Verification of P1 & P2. We verify the first and second properties of TD-CSl by validating Equations 5 and Equations 8. Since we know the position and speed of the cylinder, we can calculate the ground truth of the

³The random phase offsets in raw CSI data are removed using the method in Section 4.1.1

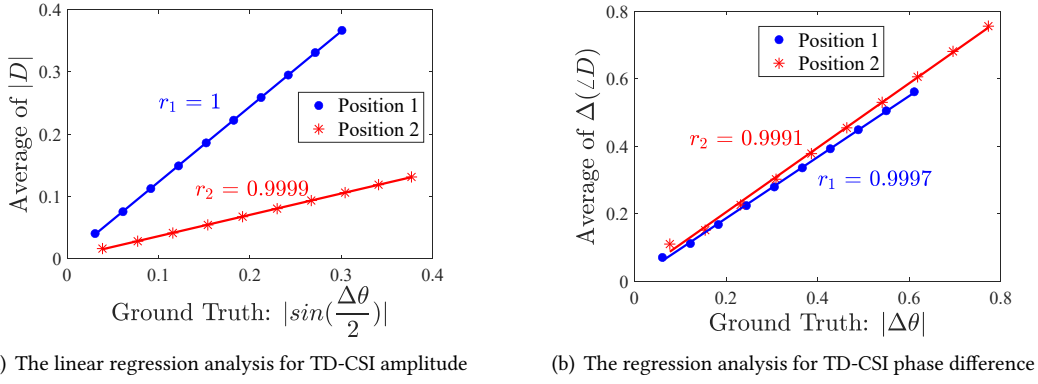


Fig. 8. Verification of P1 & P2: we perform regression analysis on the linear relationship expressed in Equations 5 and Equations 8. r_1 and r_2 represent the correction coefficients of the regression results.

Doppler speed and further obtain the $\Delta\theta(t)$ in the preceding equations. With the ground truth of $\Delta\theta(t)$, we can verify the following: (1) the linear relationship between the amplitude of TD-CSI and $|\sin \frac{\Delta\theta(t)}{2}|$; (2) the linear relationship between the phase difference of TD-CSI and $\Delta\theta(t)$. To achieve this, we perform regression analysis of the preceding linear relationships.

Figure 8 shows the results of the linear regression analysis. To mitigate the impact of noise, each data point in Figure 8 represents the average of 1200 TD-CSI amplitude or phase differences collected at the same target speed. In the experiments, the metal cylinder moves at various speeds for a minimum duration of 0.75 seconds. With a sampling rate of 400 Hz, at least 300 CSI samples are collected in each experiment. Each experiment is repeated four times, providing 1200 samples to average for each data point. We believe the close-to ideal linear regression results shown in Figure 8 are owing to the strong signal reflection from the metal cylinder and large number of samples adopted for noise mitigation. Specifically, Figure 8(a) shows the linear regression between the average TD-CSI amplitude and $|\sin \frac{\Delta\theta(t)}{2}|$ when the target moves at different speeds. We can observe that a strong linear relationship exists between the amplitude and $|\sin \frac{\Delta\theta(t)}{2}|$. Note that the slope of the regression line (corresponding to $2A$ in Equations 5) varies when the target's position changes. On the other hand, Figure 8(b) shows the linear regression between the average TD-CSI phase difference and $\Delta\theta(t)$. We can also observe that a strong linear relationship exists between the phase difference and $\Delta\theta(t)$. Furthermore, the slope of the regression line is always close to 1 regardless of which of the two positions the target is located. This demonstrates that the phase difference of TD-CSI can be directly used as an estimate of $\Delta\theta(t)$.

From the preceding experiment results we can see that: (1) Both the amplitude and phase of TD-CSI can reflect the Doppler speed of the target. (2) Equations 5 and Equations 8 are correct in practice. (3) The phase difference of TD-CSI can be directly used to estimate the Doppler speed of the target, while the amplitude-based Doppler speed estimation requires additional parameters.

3.5.2 Verification of P3. To verify the third property of TD-CSI, we use various time intervals to construct multiple TD-CSI signals from the same set of CSI data. Specifically, we construct TD-CSI signals from CSI data collected when the cylinder starts at position 2 and moves at a speed of 10 cm/s. As the CSI sampling rate is 400 Hz, we construct a total of 100 TD-CSI signals using time intervals ranging from 0.0025 s to 0.25 s. We quantify the impact of noise on the phase of TD-CSI using the average error between the phase difference of

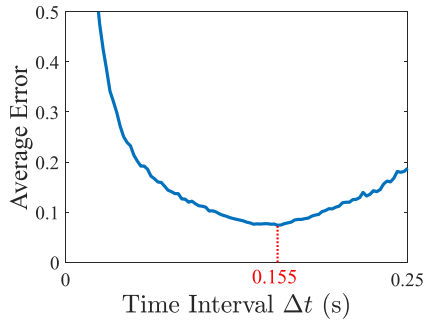


Fig. 9. Verification of P3: we use various time intervals to construct multiple TD-CSI signals, and calculate the average error between the phase difference of the TD-CSI signals and the ground truth of $\Delta\theta(t)$.

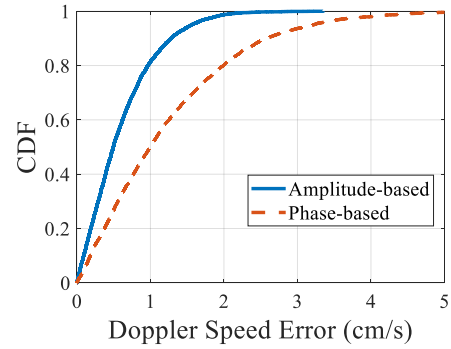


Fig. 10. Verification of P4: the cumulative distribution functions of the errors in the amplitude-based and phase-based Doppler speed estimation using TD-CSI.

TD-CSI and the ground truth of $\Delta\theta(t)$. The ground truth of $\Delta\theta(t)$ can be calculated with the known position and speed of the cylinder.

As shown in Figure 9, we can observe that noise has distinctly different impacts on TD-CSI signals constructed with different time intervals. When the time interval is set to 0.155 s, the error between the phase difference and the ground truth of $\Delta\theta(t)$ is at its lowest. This is because when the time interval is 0.155 s, $\Delta\theta(t)$ is close to π and the impact of noise on the phase of TD-CSI is minimized, as expressed in Equation 10. This result confirms the third property of TD-CSI as well as Equation 10 are correct.

3.5.3 Verification of P4. To compare the impact of noise on the Doppler speed information in the TD-CSI amplitude with that in the TD-CSI phase, we calculate the errors in the amplitude-based Doppler speed estimation and those in the phase-based estimation. We use carefully selected time intervals to construct less noisy TD-CSI signals in various settings. The slopes obtained from the preceding linear regressions offer the parameters required by the amplitude-based estimation. Figure 10 demonstrates the Cumulative Distribution Functions (CDFs) of the errors in the amplitude-based and phase-based estimation. We can observe that the error in the amplitude-based estimation is significantly lower than that in the phase-based estimation. This result corroborates the fourth property of TD-CSI, as expected.

In summary, the results of the benchmark experiments validate the four properties of the TD-CSI model. With the practical TD-CSI model, we are able to achieve accurate Doppler speed estimation while significantly reducing the number of CSI samples, approaching the theoretical lower bound, as presented in Section 4.

4 FEWSENSE: A FEW-SAMPLE DOPPLER SPEED ESTIMATION FRAMEWORK

In this section, we present FewSense, an innovative framework that accurately estimates Doppler speeds using few CSI samples. Based on the TD-CSI model, FewSense takes raw CSI samples collected from commodity WiFi devices as input and outputs precise Doppler speed estimates that can be used in various WiFi sensing applications. Figure 11 shows the workflow of FewSense, which consists of two modules:

- **TD-CSI Construction Module.** In this module, FewSense uses the input raw CSI samples to construct a TD-CSI signal. First, FewSense removes the phase offsets at raw CSI samples induced by synchronization between the transmitter and receiver. Next, FewSense constructs TD-CSI candidates using two CSI samples

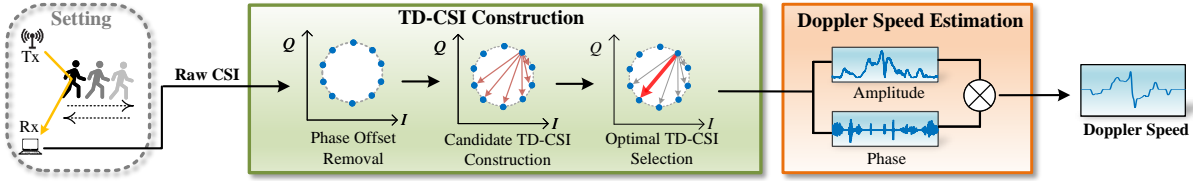


Fig. 11. The schematic workflow of FewSense.

with varying time intervals in between. FewSense then selects the TD-CSI signal with the lowest noise from the candidate pool for subsequent Doppler speed estimation.

- **Doppler Speed Estimation Module.** With the selected TD-CSI signal, we propose to use both amplitude and phase information of the TD-CSI signal to accurately estimate Doppler speed. Specifically, FewSense leverages TD-CSI phase to acquire the parameters required for amplitude-based Doppler estimation. These parameters are used to obtain more accurate Doppler speed estimates with TD-CSI amplitudes which are less affected by noise (proved in Section 3.3).

4.1 TD-CSI Construction

4.1.1 Removing the Phase Offsets in Raw CSI. Raw CSI samples collected from commodity WiFi devices suffer from random phase offsets, such as CFO (Channel Frequency Offset) and SFO (Sampling Frequency Offset) [37] due to the unsynchronization of transmitter and receiver. To remove the phase offsets, FewSense applies the phase-restoration algorithm proposed in MultiSense [44].

4.1.2 Constructing Candidate TD-CSI Signals with Varying Time Intervals Between CSI Samples. To construct a CSI difference, i.e., TD-CSI signal for Doppler speed estimation, we need two CSI samples. As indicated in Equation 10, the accuracy of Doppler speed estimation is related to the dynamic phase variation ($\Delta\theta$) and $\Delta\theta = -\frac{2\pi v_d \Delta t}{\lambda}$, thus, the estimation accuracy is related to Δt , i.e., the time interval between the two CSI samples. Based on Equation 10, we know that highest accuracy can be achieved when $\Delta t = \frac{\lambda}{2|v_d|}$ because now $|\sin \frac{\Delta\theta}{2}| = 1$. Therefore, to achieve the highest estimation accuracy, Δt should be set to $\frac{\lambda}{2|v_d|}$, i.e., the optimal value. Unfortunately, the Doppler speed v_d is unknown beforehand.

To address this issue, FewSense employs different time intervals to construct multiple candidate TD-CSI signals. To ensure we can select a candidate interval close to the optimal value, we first determine the range of the candidate interval. For applications such as human walking and gesture tracking, targets move at speeds ranging from 0.1 m/s to 5 m/s. The corresponding optimal interval ranges from 0.005 s to 0.2 s. Thus, we restrict the candidate interval in the range of 0.005 – 0.2 s. Considering that CSI samples are discrete, the number of possible intervals within the range of 0.005 – 0.2 s is limited. For example, when the sampling rate of CSI is 50 Hz, we have $\lceil(0.2 - 0.005) \cdot 50\rceil = 10$ possible intervals. We can then enumerate all possible intervals within the range to construct candidate TD-CSI signals. Note that constructing candidate TD-CSI signals would not cause a heavy computational load for FewSense since the difference operation and the subsequent variance calculation are both very light-weight.

4.1.3 Selecting the Candidate TD-CSI Signal with the Lowest Phase Noise. Based on Equation 10, the candidate TD-CSI signal with an interval closest to the optimal value $\frac{\lambda}{2|v_d|}$ exhibits the lowest phase noise among all candidate TD-CSI signals. FewSense uses the variance of the phase difference (i.e., the variance of $\Delta(\angle D(t))$) as the metric to evaluate the phase noise level for candidate selection. Specifically, FewSense calculates the

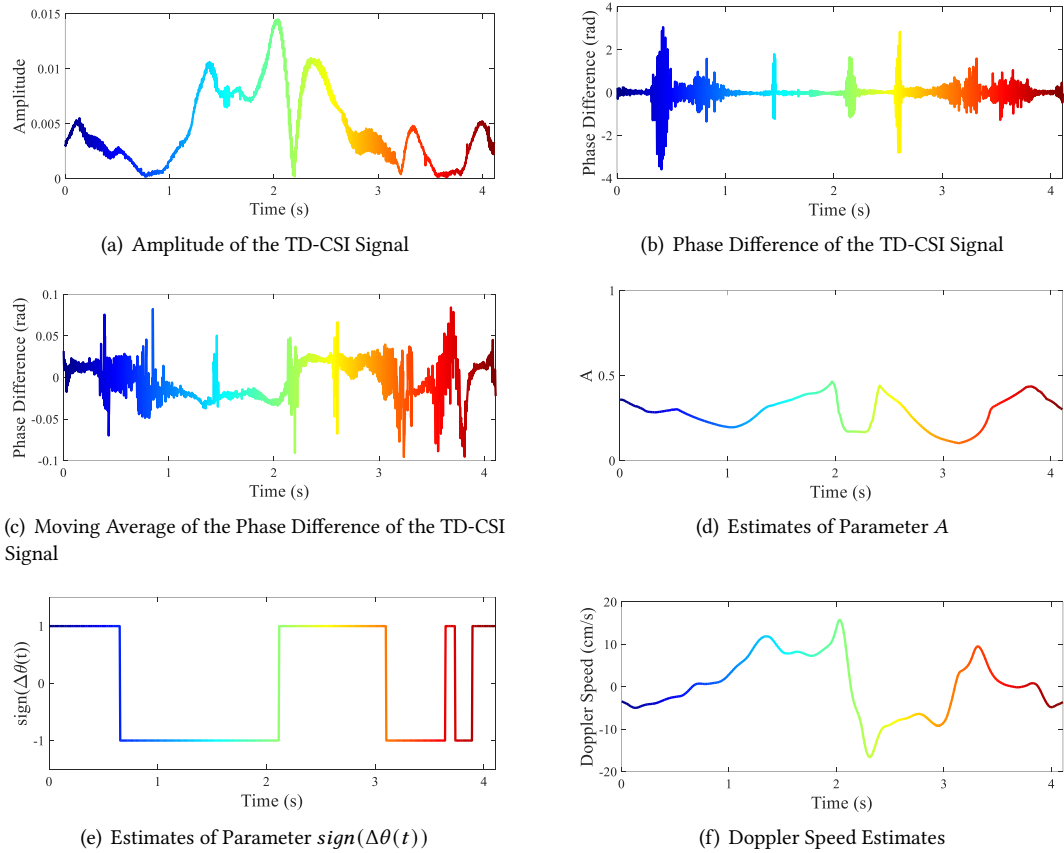


Fig. 12. An example of extracting high-precision Doppler speed estimates by combining the amplitude and phase difference of TD-CSI.

variance of the phase difference for each candidate TD-CSI signal and selects the candidate TD-CSI signal with the minimum variance.

4.2 Doppler Speed Estimation

In this module, we combine information extracted from both amplitude and phase of the selected TD-CSI signal to obtain high-precision Doppler speed estimates.

In Section 3.3, we show that both TD-CSI amplitude and phase contain the Doppler speed information. While the Doppler information contained in TD-CSI amplitude is more accurate, it requires extra parameters to obtain the true Doppler estimates. We propose to use TD-CSI phase information to help extract the parameters required for amplitude-based Doppler estimation. Specifically, we combine both amplitude and phase of TD-CSI to estimate the parameters required by Doppler speed estimation using the amplitude of TD-CSI.

As deduced in Section 3.3, the phase difference of TD-CSI provides an unbiased estimate of $\Delta\theta(t)$, i.e., $\Delta\theta(t) = E(\Delta(\angle D(t)))$, where $E(\Delta(\angle D(t)))$ denotes the expected value of the phase difference of TD-CSI. With Equation 5, we can express the correlation between the amplitude and phase difference as $|D(t)| = 2A|\sin \frac{E(\Delta(\angle D(t)))}{2}| + \epsilon_a(t)$.

Then the parameter A can be estimated as

$$\hat{A} = \frac{|D(t)|}{2|\sin \frac{\overline{\Delta(\angle D(t))}}{2}|}, \quad (12)$$

where $\overline{\Delta(\angle D(t))}$ represents the average of the phase difference of TD-CSI within a time window. The other parameter $\text{sign}(\Delta\theta(t))$ can also be acquired from the phase difference of TD-CSI. As $\Delta\theta(t) = E(\Delta(\angle D(t)))$, we can take $\overline{\text{sign}(\Delta(\angle D(t)))}$ as an estimate of $\text{sign}(\Delta\theta(t))$.

Note that extracting the value of parameter A involves the noisier phase difference of TD-CSI. One may ask why the obtained A value is accurate enough to be used for Doppler estimation. This is because A can be assumed as a constant within a short period of time as expressed in Equation 1. Therefore, we can apply a sliding average operation to mitigate the effect of noise on the estimation of A value. FewSense then inputs the estimated parameter A and $\text{sign}(\Delta\theta(t))$ as well as the amplitude of TD-CSI into Equation 7 for high-precision Doppler speed estimates.

In the implementation, FewSense uses a window of 0.1 s to calculate the average of $\Delta\theta(t)$, which enables the determination of $\text{sign}(\Delta\theta(t))$ and a coarse estimate of A . Then, a window of 0.4 s is employed to calculate the sliding average of A . Finally, FewSense produces high-precision Doppler speed estimates utilizing the amplitude of TD-CSI, A , and $\text{sign}(\Delta\theta(t))$, as expressed in Equation 7. To further reduce noise in Doppler speed estimates, FewSense can average Doppler speed estimates across all sub-carriers and antennas. In our implementation, FewSense first extracts the Doppler speed estimates using a few CSI samples from each sub-carrier received by each antenna. Subsequently, it averages a total of $30 \times 3 = 90$ Doppler speed estimates from different sub-carriers and antennas to mitigate noise. We demonstrate the process of estimating Doppler speeds using the selected TD-CSI signal with an example in Figure 12.

5 EVALUATION

In this section, we evaluate the Doppler speed estimation performance of FewSense through benchmark experiments and a real-world case study. Benchmark experiments are conducted to validate the effectiveness of FewSense under various conditions and study the impact of different processing and parameters. In the case study, we apply FewSense to realize walking trajectory tracking in real-world scenarios. We compare FewSense with the state-of-the-art in terms of Doppler speed estimation accuracy. We further utilize the Doppler speeds estimated to reconstruct the walking trajectories, demonstrating the practicality and robustness of FewSense.

5.1 Experiment Setup

WiFi Packet Transmission. We use GigaByte mini PC equipped with an Intel 5300 wireless NIC to transmit and receive WiFi packets. The transmitter is equipped with one antenna and operates in the injection mode. The receivers are equipped with three antennas and operate in the monitor mode. The central frequency and bandwidth of the WiFi signal are set to 5.50 GHz and 40 MHz, respectively.

CSI Collection & Processing. The open-source Linux CSI tool [11] is installed at the receivers for CSI data collection. The collected CSI data is sent to a laptop with an Intel i7-9750H CPU and 16GB RAM for data processing. MATLAB R2022a is utilized to process the data.

5.2 Benchmark Experiments

Experiment Setting. As shown in Figure 13, we employ a metal cylinder (ideal signal reflector) as the target⁴ in the benchmark experiments. The metal cylinder has a diameter of 20 cm and a height of 20 cm. We use a

⁴Experiments with human target will be presented in the case study section.

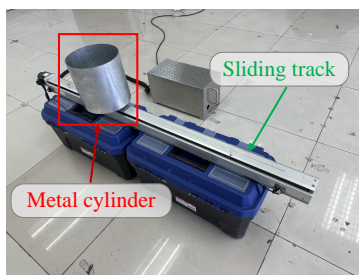


Fig. 13. The metal cylinder placed on a high-precision sliding track.

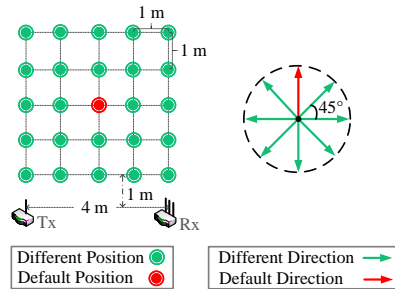


Fig. 14. Illustration of the positions and directions of the metal cylinder's movements.

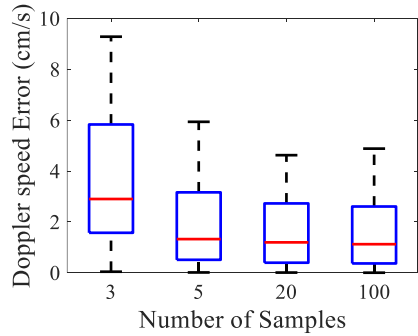


Fig. 15. Doppler speed estimation using different numbers of CSI samples.

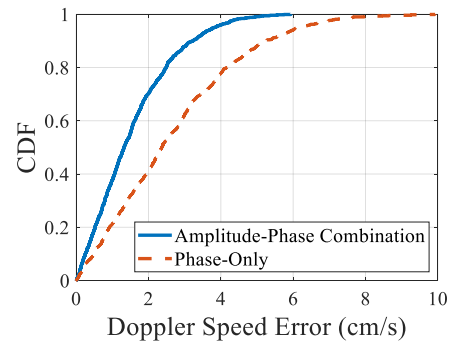


Fig. 16. Improvement of amplitude-phase combination.

1.2 m-long sliding track with a digital controller to move the metal cylinder precisely. A transmitter and a receiver are placed 4 m apart to collect CSI data. We place the metal cylinder at different positions and move it along different directions, as shown in Figure 14. In each experiment, the metal cylinder moves at speeds of 10 cm/s, 20 cm/s, and 30 cm/s, respectively. We repeat the experiment five times at each position and each direction.

Ground Truth. We use the digital controller to set the moving speed of the metal cylinder on the high-precision sliding track. We calculate the ground truth Doppler speed of the metal cylinder using its moving speed and its position with respect to the transceiver pair.

5.2.1 Doppler Speed Estimation using Different Numbers of CSI Samples. We first investigate the impact of number of CSI samples on Doppler speed estimation. We calculate one Doppler speed estimate of the metal cylinder every 0.25 s. By adjusting the packet transmission rate, we can vary the number of CSI samples obtained within 0.25 s. In our four sets of experiments, we acquire 100, 20, 5, and 3 CSI samples to calculate a Doppler speed estimate, respectively. Note that we average Doppler speed estimates across 30 sub-carriers and 3 antennas to further reduce the noise in the estimates. Figure 15 shows the Doppler speed estimation error of FewSense for different numbers of CSI samples. When we reduce the number of samples from 100 to 5, we observe that the median error of FewSense remains around 1.3 cm/s. Even with only 3 samples (the theoretical lower bound we prove in Section 3.4) for Doppler speed estimation, FewSense still achieves a low median error of 2.9 cm/s.

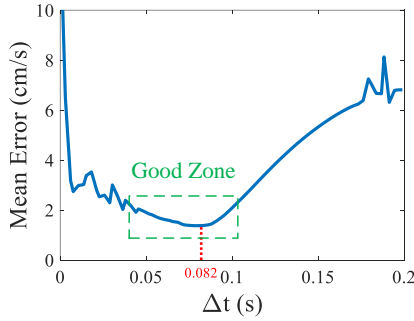


Fig. 17. Impact of different time intervals.

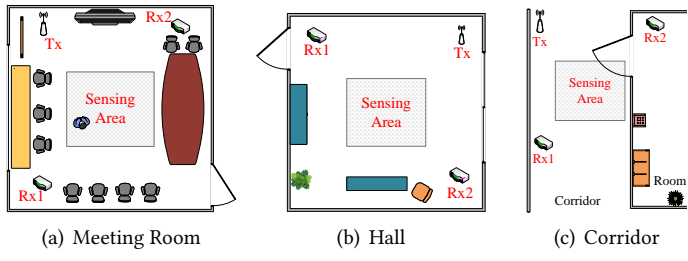


Fig. 18. Illustration of experiment settings in three typical real-world environments.

5.2.2 Amplitude-Phase Combined Estimation vs. Phase-Only Estimation. As described in Section 4.2, FewSense combines the amplitude and phase of TD-CSI to improve the accuracy of Doppler speed estimation. Taking five CSI samples as the example, we evaluate the improvement achieved by the amplitude-phase combination compared to the method using only the phase. Note that Doppler speed can not be obtained with only amplitude. Both two methods employ the same TD-CSI signal constructed to estimate the Doppler speed. As shown in Figure 16, the median errors of the amplitude-phase combined method and phase-only method are 1.32 cm/s and 2.37 cm/s, respectively. The 44.3% median error reduction indicates that combining the amplitude and phase of the TD-CSI signal can effectively improve the Doppler speed estimation accuracy.

5.2.3 Impact of Different Time Intervals Between CSI Samples. As concluded in Section 4.1.2, the time interval Δt employed for TD-CSI construction affects the accuracy of Doppler speed estimation. We now investigate the impact of Δt on estimation accuracy. We control the metal cylinder to move with a Doppler speed of 33.2 cm/s. We employ different Δt to construct multiple TD-CSI signals for Doppler speed estimation. Figure 17 shows the mean error of the Doppler speed estimates for different Δt . We can observe that using the optimal time interval (0.082 s) does significantly improve the estimation accuracy. This result demonstrates the correctness of selecting the candidate time interval that is closest to the optimal value. On the other hand, there is a ‘good zone’ (marked by the green box in Figure 17) where the specific value of Δt has a limited impact on the accuracy. Therefore, even if Δt selected by FewSense deviates slightly from the optimal value, FewSense can still achieve high estimation accuracy.

5.3 Case Study

In this subsection, we build a prototype passive tracking system based on FewSense. Through comprehensive human tracking experiments, we demonstrate the superiority of FewSense and validate the robustness of the prototype system under various experimental conditions.

Experiment Settings. We conduct walking trajectory tracking experiments in three typical real-world environments: a meeting room ($6.8 \text{ m} \times 7.2 \text{ m}$), a hall ($7.4 \text{ m} \times 7.8 \text{ m}$), and a corridor ($4.8 \text{ m} \times 8.5 \text{ m}$), as depicted in Figure 18. The meeting room is a multipath-rich environment with furniture (e.g., chairs and table), as shown in Figure 19. The hall is more spacious, whereas the corridor is narrow, further complicated by a wall obstructing the LoS path of the transceiver pair. We mount one transmitter and two receivers in each environment. The location of the transceivers and sensing area ($3.5 \text{ m} \times 3.5 \text{ m}$) are marked in Figure 18. We recruit 10 participants (6 males and 4 females) aged between 19 and 42, with heights ranging from 160 cm to 187 cm. Each participant walks along 5 different predefined trajectories as shown in Figure 20 for five times in all three environments. The CSI



Fig. 19. The experiment setting in the multipath-rich meeting room.

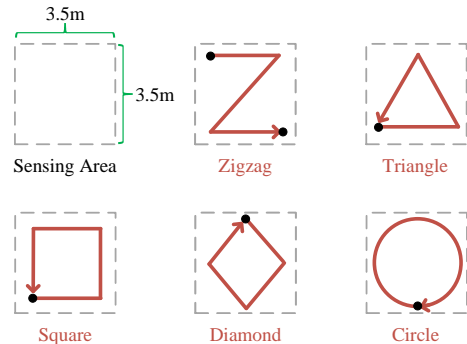


Fig. 20. Five different walking trajectories.

sampling rate is configured at 1000 Hz and we obtain different numbers of CSI samples in different experiments by down-sampling. By default, we down-sample the collected CSI data to 100 Hz for input into our system.

Ground Truth. We deploy HTC VIVE Cosmos [2] for ground truth acquisition. VIVE Cosmos utilizes laser lights to achieve localization and tracking accuracy of 1.5 mm. By affixing the VIVE handle to the target, we are able to obtain the ground truth of the walking trajectories and also compute the ground truth of target Doppler speeds with respect to the transceiver pairs.

Tracking Method. We reconstruct the walking trajectories based on the Doppler speeds estimated from two pairs of transceivers. We apply the same scheme as WiTraj [34] to convert the Doppler speeds into the target's trajectories. Specifically, we assume the initial geometric position of the target is known. Note that the raw Doppler speed is the reflection path length change speed. By leveraging the geometric relationship between the target and transceivers, we can convert the path length change speed into the radial speed of the target with respect to the transceivers [19]. With another pair of transceivers, we obtain another radial speed. By fusing the two speeds, we can obtain the true target velocity [19]. We can then calculate the next target position and iteratively compute the future positions.

5.3.1 Comparison with the State-of-the-Art in Terms of Doppler Speed Estimation. To demonstrate the superiority of FewSense, we conduct experiments to compare Doppler speed estimations using FewSense with those using state-of-the-art methods, including the Doppler estimation methods employed in IndoTrack [16], Widar2.0 [23], and WiTraj [34].

For each method, we use CSI samples within a time window of 0.2 s to calculate a Doppler speed estimate. By downsampling, we calculate a Doppler speed estimate using 200, 40, and 10 samples, respectively. Figure 21 shows the Cumulative Distribution Functions (CDFs) of Doppler speed estimation errors for the four methods under three different CSI sample numbers. Specifically, when using 200 CSI samples to obtain a Doppler speed estimate, the median Doppler speed estimation errors of FewSense, WiTraj, Widar2.0, and IndoTrack are 7.82 cm/s, 15.91 cm/s, 13.95 cm/s, and 26.14 cm/s, respectively. When using 10 CSI samples, the median errors are 9.31 cm/s, 31.84 cm/s, 24.68 cm/s, and 38.11 cm/s, respectively.

It can be observed that FewSense consistently achieves the highest Doppler speed estimation accuracy across different numbers of samples, while the performance of all three state-of-the-art methods significantly degrades with fewer CSI samples. IndoTrack exhibits a low accuracy in Doppler speed estimation due to its unsophisticated method of eliminating the static component. An insufficient number of samples can further contribute to IndoTrack's inability to accurately eliminate the static component. Widar2.0 employs a maximum-likelihood approach to discriminate multiple paths and estimates the Doppler speed of the target path. The path discrimination error

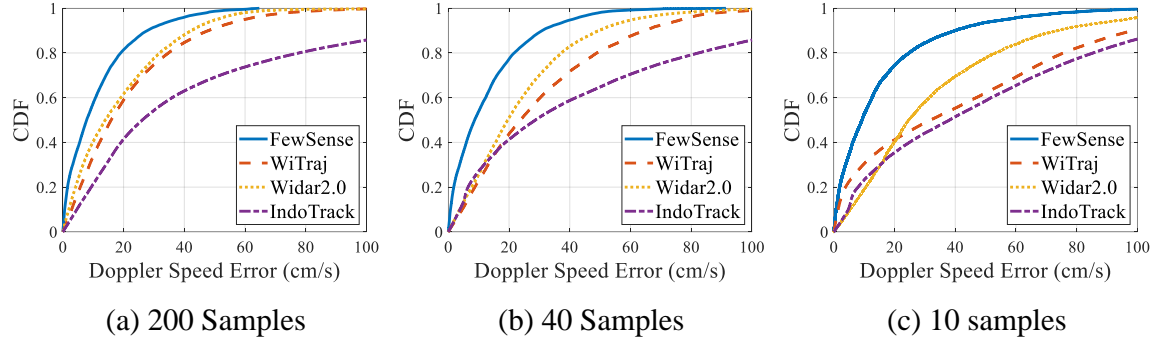


Fig. 21. Comparison with the state-of-the-art methods. Note that we compare the Doppler speed error rather than the tracking error for fairness.

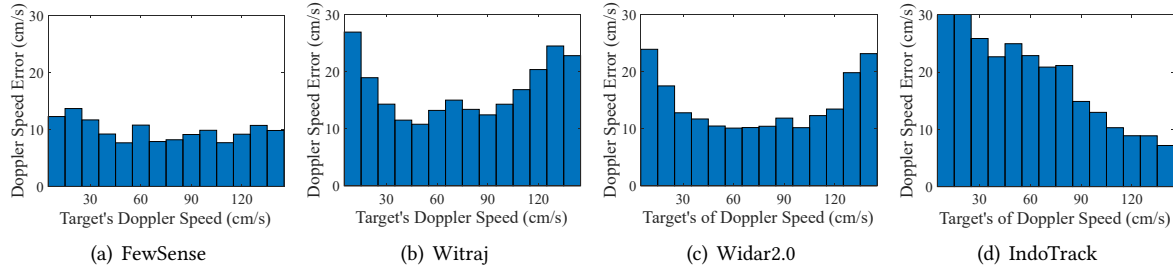


Fig. 22. Relationship between the median errors and the target's Doppler speed range when a large number of samples are used for estimation.

of Widar2.0 significantly increases when the number of CSI samples decreases. WiTraj employs only phase information to estimate Doppler speeds. When the number of CSI samples decreases, WiTraj exhibits a significant decrease in its accuracy. In contrast, FewSense efficiently eliminates the static CSI component by the differencing operation and exploits both the amplitude and phase information for high-precision Doppler speed estimation.

To explain why FewSense outperforms the state-of-the-art methods even when the number of samples is large (i.e., 200 samples), we further study the relationship between the Doppler speed estimation error and the target's Doppler speed range. The experiment result shows that the target's Doppler speed range is another key factor, besides the number of samples, that affects the accuracy of the state-of-the-art methods. Without a dynamic time window, the state-of-the-art methods work well within a small Doppler speed range. When the range increases, the performance degrades. We can see in Figure 22 that previous methods maintain low errors within a small range of Doppler speed. When there is a significant change in the Doppler speed, the estimation errors increase significantly. In contrast, our method maintains low errors across a large Doppler speed range.

Based on Equation 10 in the paper, the accuracy of phase-based Doppler speed estimation is related to the amount of phase change $\Delta\theta(t)$. Specifically, when $\Delta\theta(t) = \pi$, the CSI difference is maximized, and the impact of noise on the phase of the CSI difference is minimized. Since prior methods estimate Doppler speed based on a fixed time interval, the amount of dynamic phase change may significantly deviate from the optimal value, leading to an error increase. More importantly, due to the absence of theoretical analysis on the relationship

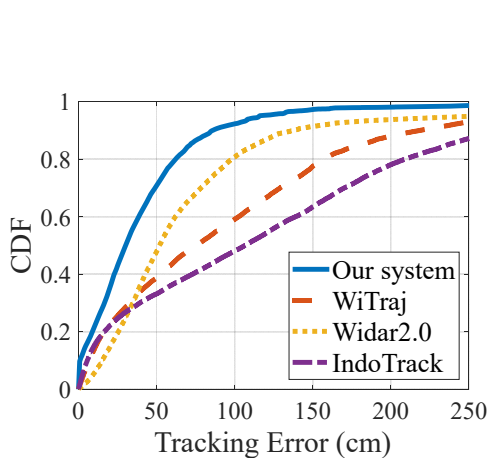


Fig. 23. Tracking performance comparison with the state-of-the-art methods.

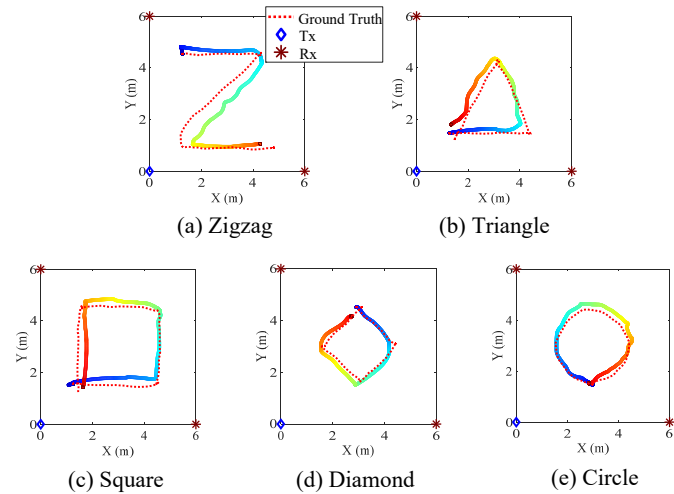


Fig. 24. Examples of our system's tracking results.

between the optimal time interval and the Doppler speed estimation accuracy, prior methods have no idea about how to determine an optimal time interval. Our method, on the one hand, can always adaptively adjust the time interval to ensure the dynamic phase change is close to the optimal value. Besides, our method makes the first attempt to employ both amplitude and phase for Doppler speed estimation. Our method can thus better adapt to real-world changes and achieve higher Doppler speed estimation accuracy.

5.3.2 Tracking Performance. To further validate the effectiveness of FewSense on walking trajectory tracking, we evaluate the trajectory reconstruction results of our system.

Overall Performance. Figure 23 shows the CDFs of the tracking errors of our system. The median and 90th percentile tracking error of our system are 30.1 cm and 85.8 cm, respectively. Figure 24 showcases examples of the trajectories reconstructed by our system. It can be observed that the reconstructed trajectories are highly consistent with the ground truth. These results demonstrate that our proposed method can accurately track human walking trajectories with only a small number of CSI samples. Furthermore, we compare the tracking performance of our method against the state-of-the-art methods. As shown in Figure 23, the median tracking errors of our system, WiTraj, Widar2.0, and IndoTrack are 30.1 cm, 90.5 cm, 51.8 cm, and 117.2 cm, respectively. This improvement is due to our method's capability to work with fewer samples, as well as its capability to handle varying velocities and locations, as concluded in Section 5.3.1.

Impact of Different CSI Sampling Rates. We downsample the collected CSI from 1000 Hz to 50 Hz, 100 Hz, 200 Hz, and 500 Hz as the input of our system. Since the maximum Doppler frequency magnitude of the target is around 25 Hz (consistent with normal human walking speed [14]) in our experiments, 50 Hz is the limit CSI sampling rate specified by the Nyquist sampling theorem. As shown in Figure 25, the median tracking errors are 33.70 cm, 30.15 cm, 27.96 cm, 31.34 cm, and 27.12 cm for CSI sampling rates of 50 Hz, 100 Hz, 200 Hz, 500 Hz, and 1000 Hz, respectively. The results indicate that our system performs consistently across different CSI sampling rates and works well even at the limit sampling rate specified by the Nyquist sampling theorem.

Impact of Different Speeds. To validate our system's robustness to various walking speeds, we add experiments to evaluate the effect of target speed on system performance. We consider different constant speeds (i.e., slow, normal, and fast) as well as varying speed (i.e., stop for a few seconds and vary the speed from slow to fast). As shown in Figure 26, our system can achieve high tracking accuracy in all four cases. This result shows the

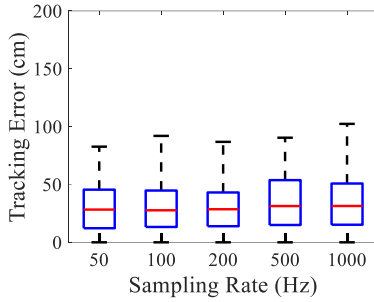


Fig. 25. Impact of CSI sampling rates.

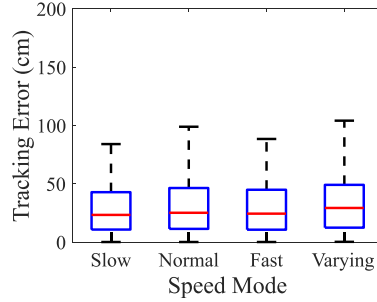


Fig. 26. Impact of user's speed modes.

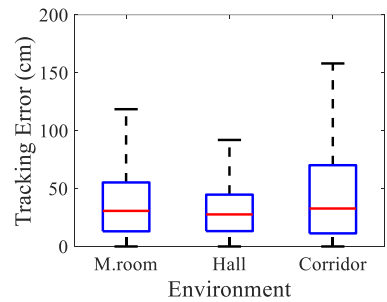


Fig. 27. Impact of environments.

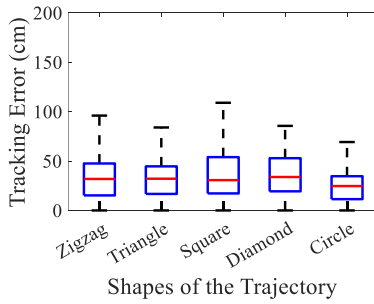


Fig. 28. Impact of trajectory shapes.

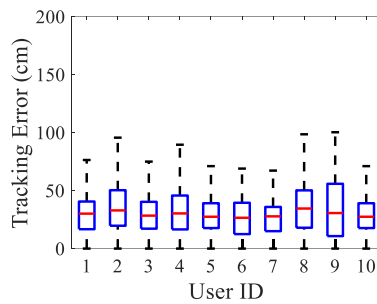


Fig. 29. Impact of user diversity.

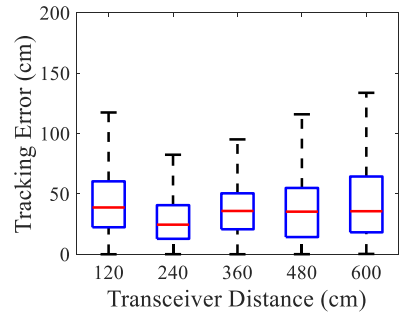


Fig. 30. Impact of transceiver distance.

adaptability of our method to a wide range of user speeds, demonstrating the potential of our system for tracking diverse human activities.

Impact of Different Environments. Figure 27 shows the tracking error of our system in the three environments. The median tracking errors in the meeting room, hall, and corridor are 30.74 cm, 27.69 cm, and 32.79 cm, respectively. We observe that the tracking errors are concentrated in a smaller range for the spacious hall. In the corridor, when a person walks into a certain part of the sensing area, the signal reflected by the human body can be blocked by the wall, resulting in a larger maximum tracking error. Despite these variations, the median tracking error remains consistent across different environments.

Impact of Different Trajectories. As shown in Figure 28, the median tracking errors for zigzag, triangle, square, diamond, and circle trajectories are 31.87 cm, 32.11 cm, 30.68 cm, 33.85 cm, and 24.69 cm, respectively. These results indicate that our system exhibits stable performance for different shapes of walking trajectories.

Impact of Different Users. Figure 29 shows the tracking error for 10 participants. Despite some variations in tracking error distributions among individuals, our system performs consistently well. This result highlights the robustness of our system against user diversity.

Impact of Different Transceiver Distances. We conduct an experiment to study the impact of different transceiver separations on the performance of our system. As illustrated in Figure 31, the transceiver distance is varied from 1.2 m to 6 m at a step size of 1.2 m. The experiment results in Figure 30 show that our system can achieve consistent high tracking accuracy at all transceiver distances. However, if we keep increasing the transceiver distance (e.g., tens of meters), we believe the sensing performance will eventually decrease. This is because when the distance is too large, we can not obtain CSI signals with a sufficiently high Signal-to-Noise-Ratio (SNR), leading to a decline of the system performance.

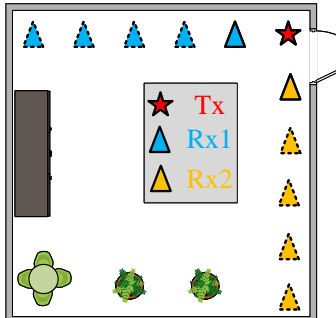
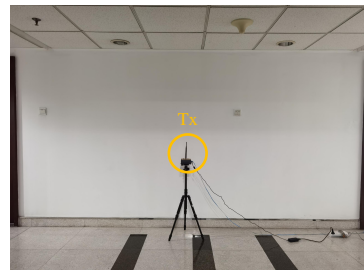


Fig. 31. The experiment settings with different transceiver distances.



(a) Transmitter placement.



(b) Receiver placements.

Fig. 32. The Non-Line-of-Sight experiment setting with the transmitter and receiver placed in different rooms with a wall in between.

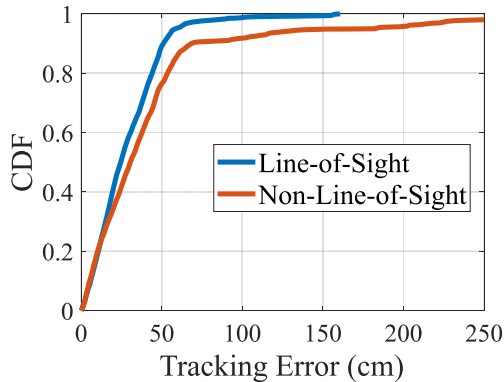
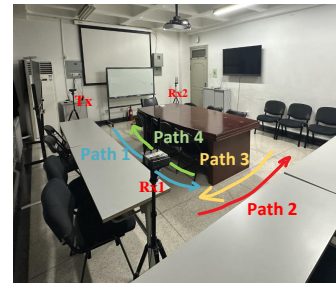
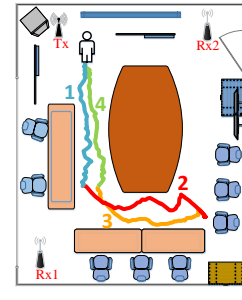


Fig. 33. Tracking performance in the NLoS environment.



(a) Meeting room with lots of furniture



(b) The reconstructed walking trajectory

Fig. 34. Restricted trajectory reconstruction in a furniture-rich environment.

Non-Line-of-Sight Environment. We conduct an experiment in a 100% Non-Line-of-Sight (NLoS) environment to study the impact of occlusion. As shown in Figure 32, the transmitter and two receivers are placed in different rooms with one wall in between. The experiment results in Figure 33 show that, although there is a notable increase in the maximum error, the overall performance of our system is only slightly degraded. We believe this is because the wall in our experiment is made of plasterboard but not solid reinforced concrete. Therefore, the signal is attenuated but not 100% blocked. We want to further point out that in the above case, the target-reflection signal is also blocked and attenuated by the wall. If only the LoS path between the transceivers is blocked by an object (e.g., furniture) and the signal path between the target and transmitter/receiver is not blocked, the performance of our system is not affected. This is because blocking the LoS path between the transceivers only affects the static path components in CSI, and we rely on the dynamic component, i.e., reflection from the target for sensing.

Restricted Trajectory in Furniture-Rich Environments. To illustrate the effectiveness of our system in furniture-rich environments, we carry out experiments in another meeting room with a size of $5.1\text{ m} \times 6.9\text{ m}$. As shown in Figure 34(a), the meeting room is filled with furniture including a big conference table ($1.2\text{ m} \times 2.4\text{ m}$), two desks, several chairs, and other items. In this environment, the target has less freedom in this room and

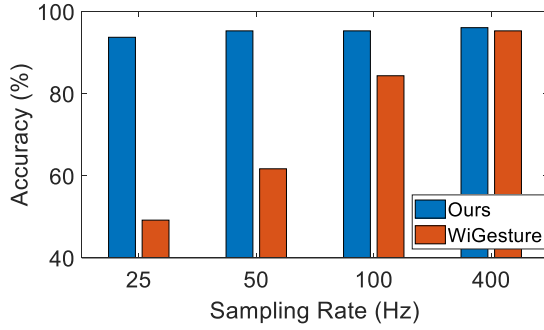


Fig. 35. Gesture recognition performance.

the target's walking trajectories are very restricted. The transmitter and receivers are placed in the corners of the room. A participant is asked to walk along four sequential paths as shown in Figure 34(a). The walking trajectory reconstructed by our system is shown in Figure 34(b). We observe that the reconstructed trajectory is quite consistent with the ground-truth. This result demonstrates the capability of our system to reconstruct the restricted walking trajectories in daily environments.

6 DISCUSSION

6.1 Multi-target Doppler Speed Estimation

Although we focus on Doppler speed estimation for a single target in this paper, we can extend our TD-CSl model to accommodate N -target scenarios as

$$D(t) = \sum_{i=1}^N 2A_i \sin \frac{\Delta\theta_i(t)}{2} e^{j(\theta_i(t) + \frac{\Delta\theta_i(t)}{2} + \frac{\pi}{2})} + \Delta\epsilon(t), \quad (13)$$

where $\Delta\theta_i = 2\pi f_i \Delta t$ and f_i is the Doppler frequency shift of the i^{th} target. Noted that the magnitude of the i^{th} -target component $|2A_i \sin (\pi f_i \Delta t)|$ is maximized when $\pi f_i \Delta t = \pi/2$. By adjusting the value of Δt , we can have one target component dominating the entire TD-CSl. Furthermore, we can amplify the TD-CSl component of each individual target one by one and extract the Doppler speed of this target. Our preliminary evaluation results show that this method works well when there is a significant difference in the velocities (either in magnitude or in direction) of multiple walking targets. However, if the velocities of two targets are very similar, our method can not separate the Doppler effects and does not work well. Despite this, we believe our model provides a new angle for multi-target sensing.

6.2 Application Scenarios

Besides walking trajectory tracking, FewSense can be applied to various other WiFi sensing applications such as gesture recognition. As an example, we conducted experiments in a setting similar to WiGesture [8] and converted the Doppler speeds estimated by FewSense into gesture results using the same method proposed by WiGesture. As shown in Figure 35, the gesture recognition system based on FewSense has achieved a significant improvement in recognition accuracy, especially in scenarios with fewer samples.

6.3 Applying Our Proposed Method on Other Wireless Signals

The model analysis and Doppler speed estimation method based on the signal difference can be applied to other wireless signals such as 4G/5G, continuous-wave radar, IQ-modulated acoustic signals, etc. Since CSI-like channel information can be obtained from many wireless signals, our proposed method has the potential to be applied to a large range of other wireless signals for Doppler speed estimation to reduce the required number of samples.

7 RELATED WORK

In this section, we review previous Doppler speed estimation works from two perspectives: WiFi-based and non-WiFi-based.

7.1 WiFi-based Doppler Speed Estimation

Early works extract coarse-grained Doppler speed information for motion recognition. WiSee [21] and WiDance [24] extract the sign of Doppler speed to recognize activities. Authors in a recent work [20] utilize the cross-zero points of Doppler speed to classify several basic arm gestures. Although these works can effectively recognize diverse large movements based on coarse-grained Doppler speed estimation, they lack the ability to sense small motions or track precise motion trajectories with fine-grained Doppler speed estimates.

Recent works [7, 8, 16, 19, 23, 33, 34, 42] further extract fine-grained Doppler speed estimates to support more applications. Pioneers attempt to apply classical algorithms for fine-grained Doppler speed estimation on WiFi. IndoTrack [16] employs a MUSIC-based method [27] to estimate Doppler speed but it requires a large number of samples as well as 360-degree phase rotation to eliminate the static component before estimation. mD-Track [38] formulates the estimation of Doppler speed and other parameters as a multi-domain parameter estimation problem and uses Expectation-Maximization (EM) algorithm [18] to tackle the problem. The EM algorithm based on the Law of Large Numbers (LLN) requires substantial samples to ensure the accuracy. Although WiDar2.0 [23] employs a high-pass filter to remove the static component, small low-speed motions are also filtered and can not be captured by WiDar2.0. PITrack [19] extracts extra Doppler speeds from increased number of transceiver pairs to improve the robustness of indoor tracking. However, it still requires samples from a large time window for accurate estimation.

Latest research proposes to estimate fine-grained Doppler speed by directly extracting features from the signal phase. FingerDraw [33] and WiTraj [34] use the CSI quotient to extract Doppler speed information for hand/human trajectory tracking. WiGesture [8] extracts the Doppler speed information to realize position-independent gesture recognition. In these works, while three samples are used in the final Doppler estimation stage, a much larger number of samples (e.g., 400 samples in WiGesture) are required in the denoising stage as the input to a Savitzky-Golay (S-G) filter. In contrast, the proposed method requires fewer samples owing to the optimal interval selected to minimize the phase error. Also, different from conventional methods only applying phase information, the proposed method involves the amplitude information, which is less affected by noise for sensing.

We believe the proposed Doppler-based system is an important complement to AoA and ToF-based solutions for localization. While Doppler information can not provide the initial position of the target but just the relative displacement, we can combine it with AoA and ToF information to obtain the absolute location of the target.

7.2 Non-WiFi-based Doppler Speed Estimation

In addition to WiFi signals, various other wireless signals have been employed to extract Doppler speed information. Dedicated radar devices [6, 26] have been used to establish a mapping between Doppler speed and fall activities. Meanwhile, WiGait [12] employs FMCW radar with high-ranging resolutions to obtain Doppler speed for estimating stride length and sensing walking gaits. Other works deploy UWB radars for imaging and gait

recognition [25, 28]. However, radar systems are typically associated with relatively high costs, substantial energy consumption, and limited integration into our daily lives.

There are other works that utilize 4G/5G, LoRa, and acoustic signals for Doppler speed estimation. An LTE-based system [4] achieves robust gesture recognition by extracting Doppler speed from 4G signals. A 5G-based sensing system [9] employs Doppler speed information to estimate user’s walking speeds. Lora-based systems have been explored [46] to sense fine-grained human activities based on Doppler speed estimation. AcousticID [40] recognizes different gaits by analyzing the Doppler effect of various body parts on acoustic signals. Although our framework may not be directly applicable to these signals, we believe the proposed methodology can inspire future research on these signals to improve the sensing performance.

8 CONCLUSION

In this paper, by exploiting the CSI difference (TD-CSI), we achieve high-precision Doppler speed estimation using few CSI samples. We establish a rigorous TD-CSI model and design a robust Doppler speed estimation framework based on the established model. Furthermore, we show that besides the conventional phase information, amplitude of CSI difference can also be utilized for Doppler speed estimation and it is actually affected less by noise. Extensive experiments demonstrate that the proposed approach can significantly relax the requirement of a large number of CSI samples while still maintaining high-precision Doppler speed estimation. We believe this is a new paradigm for Doppler speed estimation, moving one fundamental step towards the practical adoption of Doppler speed for WiFi tracking and sensing.

ACKNOWLEDGMENTS

This research is supported by NSFC A3 Project 62061146001 and PKU-NTU Collaboration Project.

REFERENCES

- [1] Giuseppe Bianchi, Luigi Fratta, and Matteo Oliveri. 1996. Performance evaluation and enhancement of the CSMA/CA MAC protocol for 802.11 wireless LANs. In *Proceedings of PIMRC’96-7th International Symposium on Personal, Indoor, and Mobile Communications*, Vol. 2. IEEE, 392–396.
- [2] Miguel Borges, Andrew Symington, Brian Coltin, Trey Smith, and Rodrigo Ventura. 2018. HTC vive: Analysis and accuracy improvement. In *2018 IEEE/RSJ International Conference on Intelligent Robots and Systems (IROS)*. IEEE, 2610–2615.
- [3] E Oran Brigham and RE Morrow. 1967. The fast Fourier transform. *IEEE spectrum* 4, 12 (1967), 63–70.
- [4] Weiyan Chen, Kai Niu, Deng Zhao, Rong Zheng, Dan Wu, Wei Wang, Leye Wang, and Daqing Zhang. 2020. Robust dynamic hand gesture interaction using LTE terminals. In *2020 19th ACM/IEEE International Conference on Information Processing in Sensor Networks (IPSN)*. IEEE, 109–120.
- [5] IEEE Computer Society LAN/MAN Standards Committee et al. 2007. IEEE Standard for Information technology-Telecommunications and information exchange between systems-Local and metropolitan area networks-Specific requirements Part 11: Wireless LAN Medium Access Control (MAC) and Physical Layer (PHY) Specifications. *IEEE Std 802.11^* (2007).
- [6] Ajay Gadge, Moeness G Amin, Yimin D Zhang, and Fauzia Ahmad. 2014. Fall detection and classifications based on time-scale radar signal characteristics. In *Radar sensor technology XVIII*, Vol. 9077. SPIE, 330–338.
- [7] Ruiyang Gao, Wenwei Li, Yaxiong Xie, Enze Yi, Leye Wang, Dan Wu, and Daqing Zhang. 2022. Towards Robust Gesture Recognition by Characterizing the Sensing Quality of WiFi Signals. *Proceedings of the ACM on Interactive, Mobile, Wearable and Ubiquitous Technologies* 6, 1 (2022), 1–26.
- [8] Ruiyang Gao, Mi Zhang, Jie Zhang, Yang Li, Enze Yi, Dan Wu, Leye Wang, and Daqing Zhang. 2021. Towards Position-Independent Sensing for Gesture Recognition with Wi-Fi. *Proceedings of the ACM on Interactive, Mobile, Wearable and Ubiquitous Technologies* 5, 2 (2021), 1–28.
- [9] Bahareh Gholampoor Yazdi, Isha Singh, and Stephan Sigg. 2017. 5G ubiquitous sensing: passive environmental perception in cellular systems. In *2017 IEEE 86th Vehicular Technology Conference (VTC-Fall)*. IEEE, 1–6.
- [10] Xiaonan Guo, Bo Liu, Cong Shi, Hongbo Liu, Yingying Chen, and Mooi Choo Chuah. 2017. WiFi-enabled smart human dynamics monitoring. In *Proceedings of the 15th ACM Conference on Embedded Network Sensor Systems*. 1–13.
- [11] Daniel Halperin, Wenjun Hu, Anmol Sheth, and David Wetherall. 2011. Tool release: gathering 802.11 n traces with channel state information. *ACM SIGCOMM Computer Communication Review* 41, 1 (2011), 53–53.

- [12] Chen-Yu Hsu, Yuchen Liu, Zachary Kabelac, Rumen Hristov, Dina Katahi, and Christine Liu. 2017. Extracting gait velocity and stride length from surrounding radio signals. In *Proceedings of the 2017 CHI Conference on Human Factors in Computing Systems*. 2116–2126.
- [13] Manikanta Kotaru, Kiran Joshi, Dinesh Bharadia, and Sachin Katti. 2015. SpotFi: Decimeter Level Localization Using WiFi. In *Proceedings of the 2015 ACM Conference on Special Interest Group on Data Communication (SIGCOMM '15)*. ACM, 269–282.
- [14] Robert V Levine and Ara Norenzayan. 1999. The pace of life in 31 countries. *Journal of cross-cultural psychology* 30, 2 (1999), 178–205.
- [15] Shengjie Li, Zhaopeng Liu, Yue Zhang, Qin Lv, Xiaopeng Niu, Leye Wang, and Daqing Zhang. 2020. WiBorder: Precise Wi-Fi based Boundary Sensing via Through-wall Discrimination. *Proceedings of the ACM on Interactive, Mobile, Wearable and Ubiquitous Technologies* 4, 3 (2020), 1–30.
- [16] Xiang Li, Daqing Zhang, Qin Lv, Jie Xiong, Shengjie Li, Yue Zhang, and Hong Mei. 2017. IndoTrack: Device-free indoor human tracking with commodity Wi-Fi. *Proceedings of the ACM on Interactive, Mobile, Wearable and Ubiquitous Technologies* 1, 3 (2017), 72.
- [17] Yang Li, Dan Wu, Jie Zhang, Xuhai Xu, Yaxiong Xie, Tao Gu, and Daqing Zhang. 2022. DiverSense: Maximizing Wi-Fi Sensing Range Leveraging Signal Diversity. *Proceedings of the ACM on Interactive, Mobile, Wearable and Ubiquitous Technologies* 6, 2 (2022), 1–28.
- [18] Todd K Moon. 1996. The expectation-maximization algorithm. *IEEE Signal processing magazine* 13, 6 (1996), 47–60.
- [19] Kai Niu, Xuanzhi Wang, Fusang Zhang, Rong Zheng, Zhiyun Yao, and Daqing Zhang. 2022. Rethinking Doppler Effect for Accurate Velocity Estimation With Commodity WiFi Devices. *IEEE Journal on Selected Areas in Communications* 40, 7 (2022), 2164–2178. <https://doi.org/10.1109/JSAC.2022.3155523>
- [20] Kai Niu, Fusang Zhang, Xuanzhi Wang, Qin Lv, Haitong Luo, and Daqing Zhang. 2021. Understanding WiFi Signal Frequency Features for Position-Independent Gesture Sensing. *IEEE Transactions on Mobile Computing* (2021), 1–1. <https://doi.org/10.1109/TMC.2021.3063135>
- [21] Qifan Pu, Sidhant Gupta, Shyamnath Gollakota, and Shwetak Patel. 2013. Whole-home gesture recognition using wireless signals. In *Proceedings of the 19th annual international conference on Mobile computing & networking*. ACM, 27–38.
- [22] Kun Qian, Chenshu Wu, Zheng Yang, Yunhao Liu, and Kyle Jamieson. 2017. Widar: Decimeter-level passive tracking via velocity monitoring with commodity Wi-Fi. In *Proceedings of the 18th ACM International Symposium on Mobile Ad Hoc Networking and Computing*. ACM, 6.
- [23] Kun Qian, Chenshu Wu, Yi Zhang, Guidong Zhang, Zheng Yang, and Yunhao Liu. 2018. Widar2. 0: Passive human tracking with a single wi-fi link. In *Proceedings of the 16th Annual International Conference on Mobile Systems, Applications, and Services*. 350–361.
- [24] Kun Qian, Chenshu Wu, Zimu Zhou, Yue Zheng, Zheng Yang, and Yunhao Liu. 2017. Inferring motion direction using commodity wi-fi for interactive exergames. In *Proceedings of the 2017 CHI Conference on Human Factors in Computing Systems*. ACM, 1961–1972.
- [25] Soumya Prakash Rana, Maitreyee Dey, Mohammad Ghavami, and Sandra Dudley. 2019. Non-contact human gait identification through IR-UWB edge-based monitoring sensor. *IEEE Sensors Journal* 19, 20 (2019), 9282–9293.
- [26] Luis Ramirez Rivera, Eric Ulmer, Yimin D Zhang, Wenbing Tao, and Moeness G Amin. 2014. Radar-based fall detection exploiting time-frequency features. In *2014 IEEE China Summit & International Conference on Signal and Information Processing (ChinaSIP)*. IEEE, 713–717.
- [27] Ralph Schmidt. 1986. Multiple emitter location and signal parameter estimation. *IEEE transactions on antennas and propagation* 34, 3 (1986), 276–280.
- [28] Masafumi Setsu and Shouhei Kidera. 2017. Super-resolution Doppler velocity estimation by Gaussian-kernel based range-Doppler conversion for UWB radar. In *2017 Progress in Electromagnetics Research Symposium-Fall (PIERS-FALL)*. IEEE, 1306–1311.
- [29] Li Sun, Souvik Sen, Dimitrios Koutsikolas, and Kyu-Han Kim. 2015. Widraw: Enabling hands-free drawing in the air on commodity wifi devices. In *Proceedings of the 21st Annual International Conference on Mobile Computing and Networking*. ACM, 77–89.
- [30] Hao Wang, Daqing Zhang, Junyi Ma, Yasha Wang, Yuxiang Wang, Dan Wu, Tao Gu, and Bing Xie. 2016. Human respiration detection with commodity wifi devices: do user location and body orientation matter?. In *Proceedings of the 2016 ACM International Joint Conference on Pervasive and Ubiquitous Computing*. ACM, 25–36.
- [31] Wei Wang, Alex X Liu, Muhammad Shahzad, Kang Ling, and Sanglu Lu. 2015. Understanding and modeling of wifi signal based human activity recognition. In *Proceedings of the 21st annual international conference on mobile computing and networking*. ACM, 65–76.
- [32] Xuanzhi Wang, Kai Niu, Jie Xiong, Bochong Qian, Zhiyun Yao, Tairong Lou, and Daqing Zhang. 2022. Placement matters: Understanding the effects of device placement for WiFi sensing. *Proceedings of the ACM on Interactive, Mobile, Wearable and Ubiquitous Technologies* 6, 1 (2022), 1–25.
- [33] Dan Wu, RuiYang Gao, Youwei Zeng, Jinyi Liu, Leye Wang, Tao Gu, and Daqing Zhang. 2020. FingerDraw: Sub-wavelength Level Finger Motion Tracking with WiFi Signals. *Proc. ACM Interact. Mob. Wearable Ubiquitous Technol* 1, 1 (2020).
- [34] Dan Wu, Youwei Zeng, Ruiyang Gao, Shengjie Li, Yang Li, Rahul C Shah, Hong Lu, and Daqing Zhang. 2021. WiTraj: robust indoor motion tracking with WiFi signals. *IEEE Transactions on Mobile Computing* (2021).
- [35] Dan Wu, Daqing Zhang, Chenren Xu, Yasha Wang, and Hao Wang. 2016. WiDir: walking direction estimation using wireless signals. In *Proceedings of the 2016 ACM international joint conference on pervasive and ubiquitous computing*. ACM, 351–362.
- [36] Rui Xiao, Jianwei Liu, Jinsong Han, and Kui Ren. 2021. Onefi: One-shot recognition for unseen gesture via cots wifi. In *Proceedings of the 19th ACM Conference on Embedded Networked Sensor Systems*. 206–219.

- [37] Yaxiong Xie, Zhenjiang Li, and Mo Li. 2015. Precise Power Delay Profiling with Commodity WiFi. In *Proceedings of the 21st Annual International Conference on Mobile Computing and Networking (MobiCom '15)*. ACM, 53–64.
- [38] Yaxiong Xie, Jie Xiong, Mo Li, and Kyle Jamieson. 2019. mD-Track: Leveraging multi-dimensionality for passive indoor Wi-Fi tracking. In *The 25th Annual International Conference on Mobile Computing and Networking*. 1–16.
- [39] Jie Xiong and Kyle Jamieson. 2013. ArrayTrack: a fine-grained indoor location system. Usenix.
- [40] Wei Xu, ZhiWen Yu, Zhu Wang, Bin Guo, and Qi Han. 2019. Acousticid: gait-based human identification using acoustic signal. *Proceedings of the ACM on Interactive, Mobile, Wearable and Ubiquitous Technologies* 3, 3 (2019), 1–25.
- [41] Moustafa Youssef, Matthew Mah, and Ashok Agrawala. 2007. Challenges: device-free passive localization for wireless environments. In *Proceedings of the 13th annual ACM international conference on Mobile computing and networking*. 222–229.
- [42] Nan Yu, Wei Wang, Alex X Liu, and Lingtao Kong. 2018. QGesture: Quantifying Gesture Distance and Direction with WiFi Signals. *Proceedings of the ACM on Interactive, Mobile, Wearable and Ubiquitous Technologies* 2, 1 (2018), 51.
- [43] Youwei Zeng, Jinyi Liu, Jie Xiong, Zhaopeng Liu, Dan Wu, and Daqing Zhang. 2021. Exploring multiple antennas for long-range WiFi sensing. *Proceedings of the ACM on Interactive, Mobile, Wearable and Ubiquitous Technologies* 5, 4 (2021), 1–30.
- [44] Youwei Zeng, Dan Wu, Jie Xiong, Jinyi Liu, Zhaopeng Liu, and Daqing Zhang. 2020. MultiSense: Enabling multi-person respiration sensing with commodity wifi. *Proceedings of the ACM on Interactive, Mobile, Wearable and Ubiquitous Technologies* 4, 3 (2020), 1–29.
- [45] Youwei Zeng, Dan Wu, Jie Xiong, Enze Yi, Ruiyang Gao, and Daqing Zhang. 2019. Farsense: Pushing the range limit of wifi-based respiration sensing with csi ratio of two antennas. *Proceedings of the ACM on Interactive, Mobile, Wearable and Ubiquitous Technologies* 3, 3 (2019), 1–26.
- [46] Fusang Zhang, Zhaoxin Chang, Kai Niu, Jie Xiong, Beihong Jin, Qin Lv, and Daqing Zhang. 2020. Exploring lora for long-range through-wall sensing. *Proceedings of the ACM on Interactive, Mobile, Wearable and Ubiquitous Technologies* 4, 2 (2020), 1–27.
- [47] Feng Zhang, Chen Chen, Beibei Wang, and KJ Ray Liu. 2018. WiSpeed: A statistical electromagnetic approach for device-free indoor speed estimation. *IEEE Internet of Things Journal* 5, 3 (2018), 2163–2177.
- [48] Xianan Zhang, Lieke Chen, Mingjie Feng, and Tao Jiang. 2022. Toward reliable non-line-of-sight localization using multipath reflections. *Proceedings of the ACM on Interactive, Mobile, Wearable and Ubiquitous Technologies* 6, 1 (2022), 1–25.

A APPENDIX

A.1 Experimental Validation of the Noise Distribution Assumption

In this section, we conduct an empirical study on the distribution of the noise $\Delta\epsilon$ in TD-CSI. We first construct TD-CSI signals using the CSI obtained from real-world experiments and then extract noise samples in TD-CSI signals through signal processing techniques. Specifically, we employ a metal cylinder as the moving target. We place the cylinder on a high-precision sliding track to control its movement. The cylinder is set to start from a known position and then move along a predefined path at a constant speed for a short distance. A pair of transceivers is deployed to collect CSI at a sampling rate of 400 Hz. To construct a TD-CSI signal that

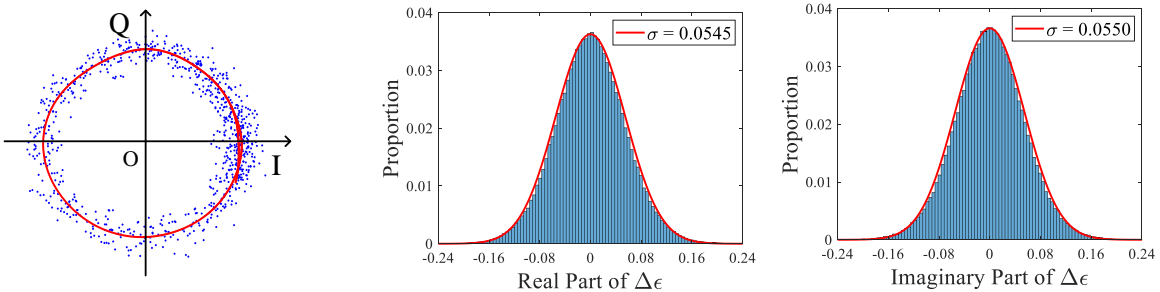


Fig. 36. Noise sample acquisition: we obtain noise samples by subtracting the noise-free TD-CSI signal (red points) from the actual TD-CSI signal (blue points).

Fig. 37. The distributions of the real and imaginary parts of the noise in TD-CSI. The blue color represents the distribution of the actual samples, and the red color represents the fitted normal distribution.

conforms to Equation 4, we first remove random phase offsets (such as CFO and SFO) from the raw CSI using the phase-restoration algorithm described in MultiSense [44]. Then, we perform a differencing operation on the restored CSI signal with a fixed time interval to obtain the TD-CSI signal. Since the metal cylinder moves at a uniform speed over a short distance, the amplitude A and phase variation $\Delta\theta(t)$ of the target-reflected signal can be approximately considered constant. Assuming there is no noise, the amplitude of the constructed TD-CSI signal, denoted as $2A|\sin \frac{\Delta\theta(t)}{2}|$, remains constant. Thus, if the constructed TD-CSI signal is noise-free, it rotates along a circle on the complex plane, as depicted by the red points in Figure 36. We apply a Savitzky-Golay (SG) filter to the actual TD-CSI signal (as depicted by the blue points in Figure 36) to derive the noise-free TD-CSI signal. Then, the noise samples within the TD-CSI signal can be calculated by subtracting the noise-free TD-CSI signal from the actual TD-CSI signal.

The distributions of the real and imaginary parts of the noise in TD-CSI are presented in Figure 37. It is shown that both the real and imaginary parts of the noise $\Delta\epsilon$ follow a zero-mean normal distribution with almost the same standard deviation, which indicates that the noise distribution is circularly symmetric. Furthermore, the covariance of the noise samples is calculated to be 2.7×10^{-5} , which is much smaller than the variance $\sigma^2 = 3 \times 10^{-3}$, so we can safely regard the covariance of the noise distribution to be zero.

A.2 Theoretical Analysis of the Average Errors of the Amplitude-based Versus Phase-based Doppler Speed Estimation

In this section, we provide a theoretical analysis of the average errors in the amplitude-based versus phase-based Doppler speed estimation. This analysis complements the discussion in Section 3.3.2.

Consistent with the analysis in Section 3.3.2, we assume that the noise $\Delta\epsilon(t)$ follows a circularly symmetric distribution (validated in Appendix A.1) and, without loss of generality, fix the amplitude of $\Delta\epsilon(t)$ as σ . Figure 38 illustrates the impact of the noise on TD-CSI in a general scenario, where the angle between the noise and the target component in TD-CSI is denoted as ϕ . ϕ is uniformly distributed between 0 and 2π . Then, the amplitude of the TD-CSI can be expressed as $|D(t)| = \sqrt{(2A \sin \frac{\Delta\theta(t)}{2})^2 + \sigma^2 - 4A\sigma \sin \frac{\Delta\theta(t)}{2} \cos \phi}$. Based on Equation 7, the average error of the amplitude-based Doppler speed estimation can be calculated as

$$AE(\widehat{|\Delta\theta(t)|}_a) = \int_0^{2\pi} \left| 2 \arcsin \sqrt{(\sin \frac{\Delta\theta(t)}{2})^2 + (\frac{\sigma}{2A})^2 - \frac{\sigma}{A} \sin \frac{\Delta\theta(t)}{2} \cos \phi - |\Delta\theta(t)|} \right| d\phi, \quad (14)$$

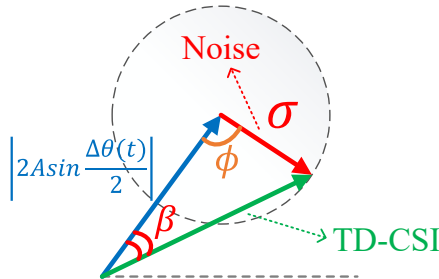


Fig. 38. Illustration of the impact of the noise on TD-CSI in a general scenario.

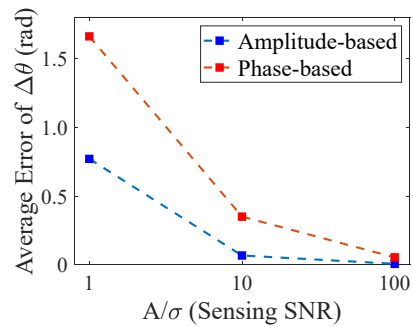


Fig. 39. Theoretical average error values of the amplitude-based and phase-based estimations across different parameters.

where $AE(\widehat{|\Delta\theta(t)|_a})$ represents the average error of the amplitude-based estimation. On the other hand, the phase shift induced by the noise can be expressed as $\beta = \arcsin(\sigma \sin \phi / \sqrt{(2A \sin \frac{\Delta\theta(t)}{2})^2 + \sigma^2 - 4A\sigma \sin \frac{\Delta\theta(t)}{2} \cos \phi})$. Since the phase-based estimation employs the difference between two TD-CSI phases to estimate Doppler speed, the estimation error can be expressed as $|\beta_1 - \beta_2|$, where β_1 and β_2 represent the phase shifts of the two TD-CSI samples. Thus, the average error of the phase-based Doppler speed estimation can be calculated as

$$AE(\widehat{\Delta\theta(t)}_p) = \int_0^{2\pi} \int_0^{2\pi} \left| \arcsin \frac{\sigma \sin \phi_1}{\sqrt{(2A \sin \frac{\Delta\theta(t)}{2})^2 + \sigma^2 - 4A\sigma \sin \frac{\Delta\theta(t)}{2} \cos \phi_1}} \right. \\ \left. - \arcsin \frac{\sigma \sin \phi_2}{\sqrt{(2A \sin \frac{\Delta\theta(t)}{2})^2 + \sigma^2 - 4A\sigma \sin \frac{\Delta\theta(t)}{2} \cos \phi_2}} \right| d\phi_1 d\phi_2, \quad (15)$$

where $AE(\widehat{\Delta\theta(t)}_p)$ represents the average error of the phase-based estimation.

Due to the complexity of the integrals involved in calculating the average errors, it is difficult to derive concise analytic expressions for the average errors. Therefore, we resort to numerical calculations to derive the average error values across different parameters. The calculations involve two independent parameters, namely $\frac{A}{\sigma}$ and $\Delta\theta(t)$. $\frac{A}{\sigma}$ represents the ratio of the target-reflected signal amplitude to the noise amplitude, serving as an indicator of Sensing Signal-to-Noise Ratio (SSNR) [32]. As indicated in Equation 2, $\Delta\theta(t)$ is related to the Doppler speed. Considering the frequent changes in target Doppler speed, we calculate the mean value of the average errors under different $\Delta\theta(t)$ to simplify our presentation of the numerical calculation results. Figure 39 shows the mean error values across different $\frac{A}{\sigma}$. It can be observed that, on average, the error in amplitude-based estimation is significantly lower than that in phase-based estimation. These results further corroborate the superior accuracy of amplitude-based estimation and motivate us to fully exploit the potential of TD-CSI by leveraging the amplitude information.